

TET-Mediated Hypermethylation Primes SDH-Deficient Cells for HIF2α-Driven Mesenchymal Transition

Aurélie Morin, Judith Goncalves, Sophie Moog, Luis-Jaime Castro-Vega, Sylvie Job, Alexandre Buffet, Marie-Joséphine Fontenille, Justine Woszczyk, Anne-Paule Gimenez-Roqueplo, Eric Letouzé, et al.

▶ **To cite this version:**

Aurélie Morin, Judith Goncalves, Sophie Moog, Luis-Jaime Castro-Vega, Sylvie Job, et al.. TET-Mediated Hypermethylation Primes SDH-Deficient Cells for HIF2α-Driven Mesenchymal Transition. Cell Reports, 2020, 30 (13), pp.4551 - 4566.e7. 10.1016/j.celrep.2020.03.022 . hal-03184305

HAL Id: hal-03184305

https://hal.sorbonne-universite.fr/hal-03184305

Submitted on 29 Mar 2021

HAL is a multi-disciplinary open access archive for the deposit and dissemination of scientific research documents, whether they are published or not. The documents may come from teaching and research institutions in France or abroad, or from public or private research centers.

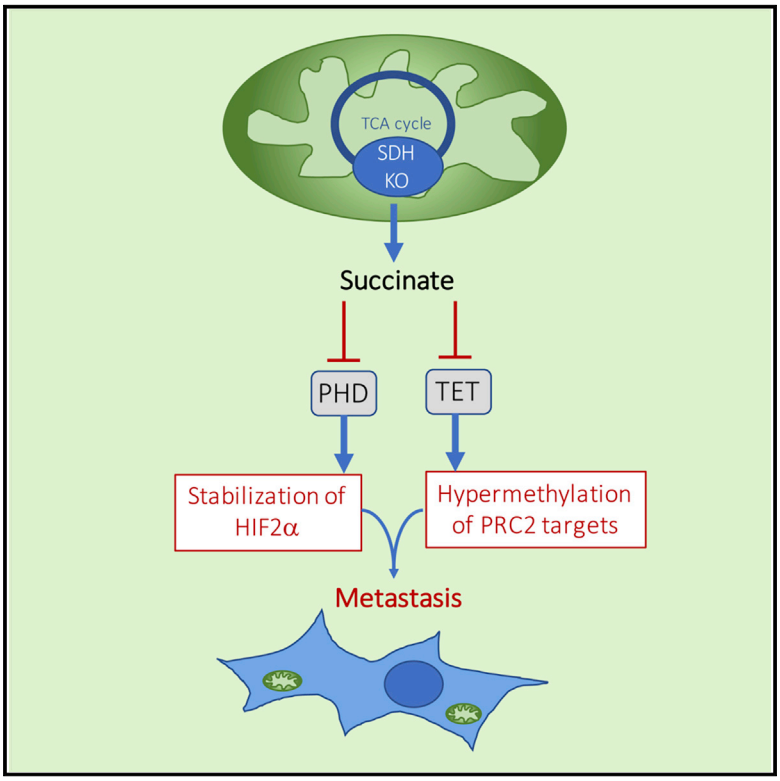
L'archive ouverte pluridisciplinaire **HAL**, est destinée au dépôt et à la diffusion de documents scientifiques de niveau recherche, publiés ou non, émanant des établissements d'enseignement et de recherche français ou étrangers, des laboratoires publics ou privés.

Article

Cell Reports

TET-Mediated Hypermethylation Primes SDH-Deficient Cells for HIF2α-Driven Mesenchymal Transition

Graphical Abstract



Authors

Aurélie Morin, Judith Goncalves, Sophie Moog, ..., Anne-Paule Gimenez-Roqueplo, Eric Letouzé, Judith Favier

Correspondence

judith.favier@inserm.fr

In Brief

Morin et al. investigate the hypermethylator phenotype of SDHB-deficient human paragangliomas and *Sdhb*$^{-/-}$ mouse cells and its link with metastatic hallmark acquisition. They reveal synergy between TET-mediated hypermethylation and pseudohypoxia that drives transition of *SDHB*-mutated tumors toward metastasis, providing a rationale for targeting HIF2α and DNA methylation in SDH-associated malignancies.

Highlights

- SDHB-mutated tumors and cells show low hydroxymethylation
- Hypermethylation in SDHB-mutated tumors preferentially affects PRC2 target genes
- TET knockdown recapitulates the hypermethylated phenotype of SDHB-deficient cells
- Combining TET inhibition and HIF2 activation mimics the SDHB metastatic phenotype

Morin et al., 2020, Cell Reports *30*, 4551–4566
March 31, 2020 © 2020 The Author(s).
https://doi.org/10.1016/j.celrep.2020.03.022

CellPress

Cell Reports
Article

OPEN ACCESS
CellPress

TET-Mediated Hypermethylation Primes SDH-Deficient Cells for HIF2α-Driven Mesenchymal Transition

Aurélie Morin,[1] Judith Goncalves,[1] Sophie Moog,[1] Luis-Jaime Castro-Vega,[1] Sylvie Job,[2] Alexandre Buffet,[1,3] Marie-Joséphine Fontenille,[1] Justine Woszczyk,[1] Anne-Paule Gimenez-Roqueplo,[1,3] Eric Letouzé,[4,5] and Judith Favier[1,5,6,*]

[1]Université de Paris, PARCC, INSERM, Equipe Labellisée par la Ligue contre le Cancer, 75015 Paris, France
[2]Programme Cartes d'Identité des Tumeurs, Ligue Nationale Contre Le Cancer, 75013 Paris, France
[3]Department of Genetics, Assistance Publique-Hôpitaux de Paris, Hôpital Européen Georges Pompidou, 75015 Paris, France
[4]Functional Genomics of Solid Tumors Laboratory, Centre de Recherche des Cordeliers, Université de Paris, INSERM, 75006 Paris, France
[5]Senior author
[6]Lead Contact
*Correspondence: judith.favier@inserm.fr
https://doi.org/10.1016/j.celrep.2020.03.022

SUMMARY

Loss-of-function mutations in the SDHB subunit of succinate dehydrogenase predispose patients to aggressive tumors characterized by pseudohypoxic and hypermethylator phenotypes. The mechanisms leading to DNA hypermethylation and its contribution to SDH-deficient cancers remain undemonstrated. We examine the genome-wide distribution of 5-methylcytosine and 5-hydroxymethylcytosine and their correlation with RNA expression in SDHB-deficient tumors and murine *Sdhb*$^{-/-}$ cells. We report that DNA hypermethylation results from TET inhibition. Although it preferentially affects PRC2 targets and known developmental genes, PRC2 activity does not contribute to the DNA hypermethylator phenotype. We also prove, *in vitro* and *in vivo*, that TET silencing, although recapitulating the methylation profile of *Sdhb*$^{-/-}$ cells, is not sufficient to drive their EMT-like phenotype, which requires additional HIF2α activation. Altogether, our findings reveal synergistic roles of TET repression and pseudohypoxia in the acquisition of metastatic traits, providing a rationale for targeting HIF2α and DNA methylation in SDH-associated malignancies.

INTRODUCTION

Succinate dehydrogenase (SDH) is the mitochondrial enzyme that catalyzes oxidation of succinate into fumarate in the tricarboxylic acid (TCA) cycle. It consists of 4 subunits encoded by the *SDHA*, *SDHB*, *SDHC*, and *SDHD* (*SDHx*) genes. Germline mutations in one of these genes predispose to pheochromocytoma and paraganglioma (PPGL), rare neuroendocrine tumors that arise in the adrenal medulla and the parasympathetic or sympathetic nervous systems, respectively. Notably, mutations in the *SDHB* gene are associated with increased risk of metastatic disease (Gimenez-Roqueplo et al., 2003) and poor prognosis (Amar et al., 2007).

Mutations affecting other TCA cycle enzymes, such as fumarate hydratase (germline mutations on *FH*) and isocitrate dehydrogenase (somatic mutations on *IDH1* or *IDH2*) are found, although infrequently, in PPGL (Castro-Vega et al., 2014; Clark et al., 2014) and often lead to other forms of cancer (Morin et al., 2014).

Mechanistically, mutations affecting SDH, fumarate hydratase (FH), or isocitrate dehydrogenase (IDH) enzymes induce accumulation of oncometabolites (succinate, fumarate, and (R)-2-hydroxyglutarate, respectively), which inhibits 2-oxoglutarate (2-OG)-dependent dioxygenases such as hypoxia-inducible factors (HIF) prolyl-hydroxylases (PHDs); ten-eleven translocation (TET) dioxygenases that hydroxylate DNA-methylated cytosines (5-methylcytosine [5mC]) into 5-hydroxymethylcytosine (5hmC), and JmjC domain-containing histone lysine demethylases (KDM). Nevertheless, the affinity of each oncometabolite for these various dioxygenases varies greatly (Rose et al., 2011), and the specific contributions of these impaired enzymatic activities in the tumor phenotype remain undetermined.

PHD inhibition results in pseudohypoxia; i.e., abnormal stabilization of HIF1α and/or HIF2α transcription factors and subsequent expression of hypoxia-inducible genes, even in normoxia. It was the first discovered oncometabolite-induced pathway. Because tumor hypoxia is a known inducer of epithelial-to-mesenchymal transition (EMT), cancer stem cell phenotypes, and metastases (Marie-Egyptienne et al., 2013), pseudohypoxia has long been considered a driver mechanism in the invasive and metastatic behavior of oncometabolite-driven tumors.

KDM and TET enzymes are involved in epigenetic regulation, which is altered in most cancers. For example, global DNA hypomethylation and specific promoter CpG island hypermethylation are hallmarks of cancer. In particular, polycomb repressive complex 2 (PRC2) targets are highly prone to cancer-specific hypermethylation (Ohm et al., 2007;

This is an open access article under the CC BY-NC-ND license (http://creativecommons.org/licenses/by-nc-nd/4.0/).

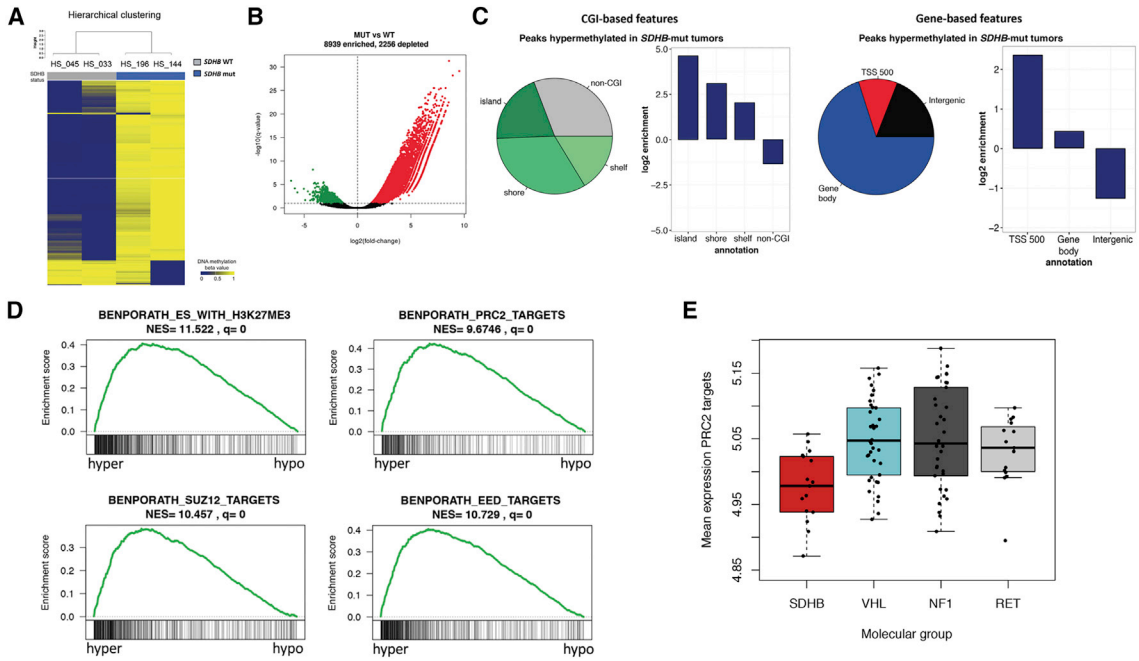


Figure 1. MeDIP-Seq Analysis of DNA Methylation in *SDHB*-mut Tumors Identifies Enrichment in PRC2 Targets

(A) Hierarchical clustering of the tumors based on methylation of the 1,000 most variant peaks.

(B) Volcano plot indicating the number of differentially methylated peaks between *SDHB*-mut and *SDHB*-wild-type (WT) PPGL.

(C) Preferential location of hypermethylated peaks in *SDHB*-mut versus *SDHB*-WT tumors and segregation in CGI-based or gene-based features.

(D) Hypermethylated peaks in *SDHB*-mut versus *SDHB*-WT tumors (identified by meDIP-seq) are strongly enriched in genes marked by H3K27me3 or targeted by SUZ12, EED, or PRC2 in ESCs (gene sets described by Ben-Porath et al. 2008). The gene set called "PRC2_targets" is composed of genes that possess the H3K27me3 mark at their promoters and are bound by SUZ12 and EED Polycomb proteins in ESCs. A description of genomic features used to analyze meDIP-seq is provided in Figure S1.

(E) Microarray-based analysis of expression of PRC2 targets in a cohort of 113 genetically determined PPGL tumors described in Letouzé et al. (2013). Middle bar, median; box, interquartile range; bars extend to 1.5 times the interquartile range.

See also Figure S1.

Schlesinger et al., 2007). PRC2 is a transcriptionally repressing complex catalyzing tri-methylation of lysine 27 of histone H3 (H3K27me3). In embryonic stem cells (ESCs), it is involved in repression of poised developmental genes (Lee et al., 2006). The PRC2 complex can also recruit the DNA methyltransferases DNMT1 and DNMT3a to its target genes (Viré et al., 2006) and has been implicated in DNA hypermethylation in cancers not driven by oncometabolites (Ohm et al., 2007; Schlesinger et al., 2007). Several studies have suggested a link between TET and PRC2 (Haffner et al., 2013; Putiri et al., 2014; Verma et al., 2018), but it remains unexplored whether PRC2 participates in DNA methylation in oncometabolites-driven tumors.

The role of TET enzymes in shaping the DNA methylome of such tumors has been partially investigated. Several groups, including ours, studied the methylome of oncometabolite-driven tumors and reported enhanced DNA methylation in (Killian et al., 2013; Letouzé et al., 2013; Lu et al., 2013) and outside CpG islands (Killian et al., 2013; Letouzé et al., 2013). However, these studies were performed using methylome arrays or reduced-representation bisulfite sequencing (enrichment in CG-rich regions), and no genome-wide, unbiased method has been used so far. Besides, the classical bisulfite conversion used in these studies is not able to distinguish 5mC from 5hmC. Global 5hmC levels in these tumors were measured using immunolabeling (Figueroa et al., 2010; Killian et al., 2013; Letouzé et al., 2013; Xiao et al., 2012), fluorescence-activated cell sorting (FACS) (Figueroa et al., 2010; Turcan et al., 2012), or dot blot (Xiao et al., 2012). These experiments showed a reduction in global levels of 5hmC that parallels the increased 5mC levels. Rampal et al. (2014) reported, in the first study published so far regarding oncometabolite-driven tumors, the genome-wide 5mC and 5hmC patterns in *TET2, WT1*, and *IDH*-mutated acute myeloid leukemia but did not assess the correlation between 5mC and 5hmC in these tumors.

In the present study, we analyze DNA methylation and hydroxymethylation along the genome in SDHB-deficient tumors. We used a tractable cellular model that recapitulates most of the phenotypic characteristics of *SDHB*-mutated tumors to determine how the pattern of hypermethylation and related transcriptional changes are established. We also provide evidence that pseudohypoxia cooperates with hypermethylation in inducing an EMT-like phenotype, suggesting synergistic requirements for tumor initiation and progression of aggressive *SDHB*-mutated tumors.

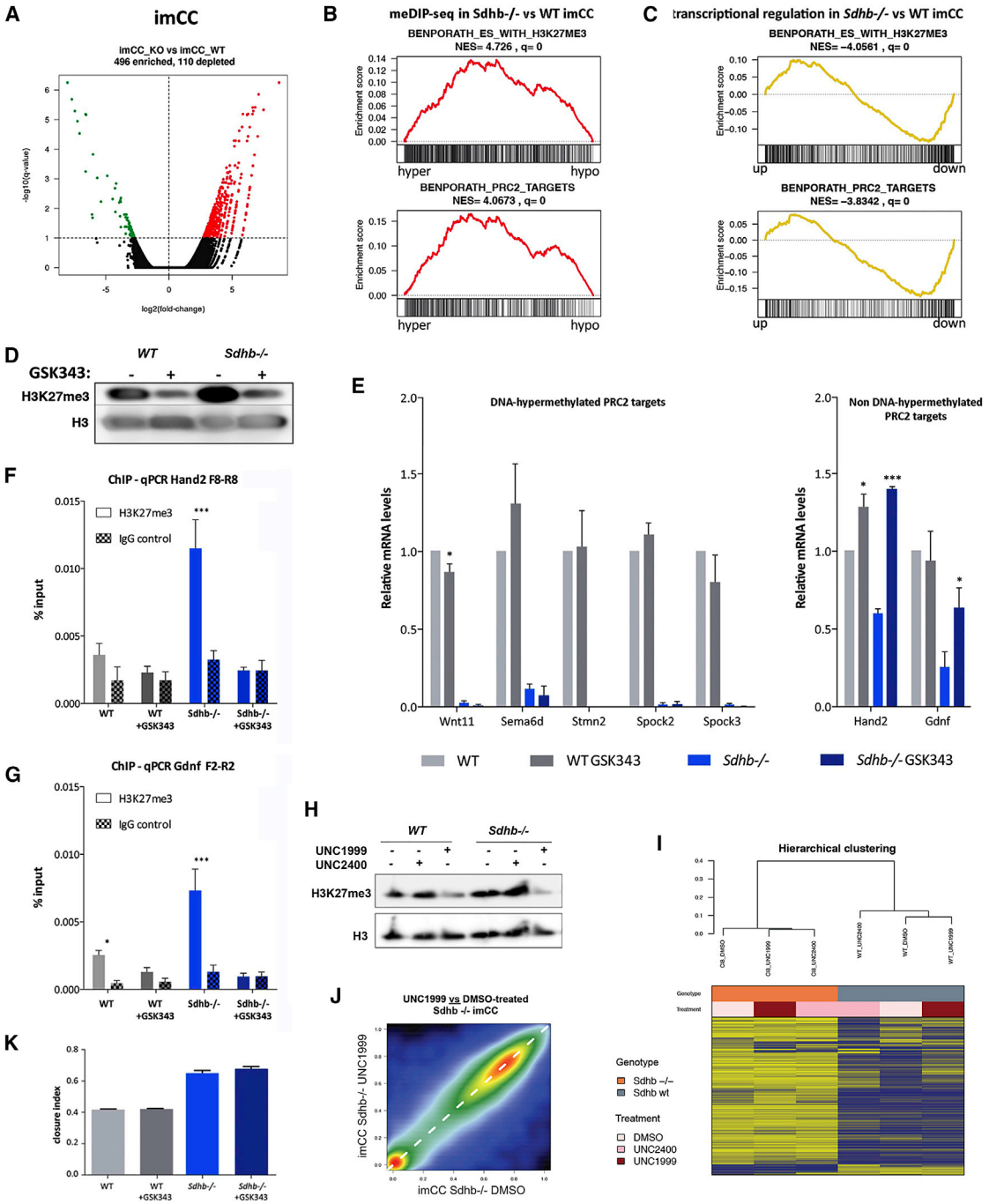


Figure 2. PRC2 Targets Are Enriched among Hypermethylated and Downregulated Genes in *Sdhb*$^{-/-}$ versus Wild-type (WT) imCCs, but PRC2 Inhibition Does Not Alter the DNA Methylation or Cell Phenotype of *Sdhb*$^{-/-}$ imCCs

(A) Volcano plot indicating the number of differentially methylated peaks between *Sdhb*$^{-/-}$ and *Sdhb*-WT imCCs.

(B) Hypermethylated peaks in *Sdhb*$^{-/-}$ compared with *Sdhb* WT imCCs (identified by meDIP-seq) are strongly enriched in genes marked by H3K27me3 or targeted by PRC2 in ESCs.

(C) Downregulated genes in *Sdhb*$^{-/-}$ compared with *Sdhb*-WT imCCs (identified in RNA sequencing [RNA-seq] data) are enriched in genes marked by H3K27me3 or targeted by PRC2 in ESCs.

(D) Inhibition of trimethylation of H3K27 by the PRC2 inhibitor GSK343 (3 μM).

(E) qRT-PCR dosage of known PRC2 targets (DNA hypermethylated or not in *Sdhb*$^{-/-}$ imCCs) in cells treated with GSK343 for 5–7 passages.

(legend continued on next page)

RESULTS

Genome-wide DNA Methylation and the PRC2 Pathway in SDHB-Deficient Tumors and Cells

Using methylation arrays and reduced-representation bisulfite sequencing (RRBS), we have previously described a hypermethylator phenotype in tumors carrying an *SDHx* mutation and in spontaneously immortalized mouse chromaffin cells (imCCs) with complete *Sdhb* knockout (Letouzé et al., 2013). To further investigate DNA methylation patterns using an un-biased and genome-wide method, we used methylated DNA Immunoprecipitation sequencing (meDIP-seq) in human PPGL carrying or not carrying *SDHB* mutations. As expected, we found strong DNA hypermethylation (80% of differentially methylated peaks) in *SDHB*-mutated (*SDHB*-mut) compared with *SDHB* wild-type (WT) tumors (Figures 1A and 1B). Hypermethylated peaks were more frequent at CpG islands (CGIs) and promoters (defined as 500 bp before and after the transcription start sites [TSSs] and hereafter referred to as TSS 500), but they were also detectable in the rest of the genome (Figures 1C and S1A).

Gene set analysis of hypermethylated genes in *SDHB*-mut tumors revealed strong enrichment in genes deregulated in cancer and in genes encoding proteins involved in pluripotency or development. The most significantly enriched sets of genes were polycomb targets and genes marked by H3K27me3 in ESCs and neural precursor cells (Figure 1D; Table S1). A heatmap of DNA methylation, established from the methylome array data from the French COMETE (COrtico et MEdullo-surrénale, les Tumeurs Endocrines) cohort (4 non-tumoral samples and 145 PPGL samples) (Letouzé et al., 2013) and restricted to the gene set BENPORATH_ES_WITH_H3K27ME3, showed strong hypermethylation in tumors carrying an *SDHx* gene mutation (Figure S1B). To address whether this hypermethylation was accompanied by reduced RNA expression, we used the transcriptomics data on the COMETE cohort of PPGL encompassing 17 *SDHB*-, 40 *VHL*-, 37 *NF1*-, and 19 *RET*-mutated PPGL samples. *SDHB*-mut tumors showed the lowest mean expression of PRC2 targets among all PPGL subgroups (Figure 1E).

We also compared expression of the PRC2 core components EZH2, SUZ12, and EED among the expression clusters described in Burnichon et al. (2011). EZH2 and SUZ12 were overexpressed in cluster C1A, which is composed of tumors with mutations on genes encoding TCA cycle enzymes (Figure S1C), whereas the PRC1 components RING1 and BMI1 were not (Figure S1D). EZH2 and SUZ12 were also overexpressed in metastatic compared with benign tumors (Figure S1E).

To investigate whether PRC2 participates in the DNA hypermethylator phenotype, we used the *Sdhb*$^{-/-}$ imCC model, which recapitulates the strong DNA hypermethylation observed by meDIP-seq in SDH tumors (Figure 2A) and the enrichment in PRC2 among hypermethylated (Figure 2B) or transcriptionally repressed genes (Figure 2C). We treated imCCs with a specific PRC2 inhibitor, GSK343, a potent and highly selective EZH2 inhibitor (Verma et al., 2012), for up to 7 passages. GSK343 treatment resulted in sustained inhibition of H3K27me3 (Figure 2D) but did not modify global 5mC levels (Figure S2A) or 5hmC levels (Figure S2B). Nevertheless, most polycomb targets downregulated in *Sdhb*$^{-/-}$ cells were also hypermethylated at their TSS 500. We thus selected seven PRC2 targets that were downregulated in *Sdhb*$^{-/-}$ cells. These genes are involved in neural differentiation (Hand2 [Stanzel et al., 2016], Gdnf [Roussa and Krieglstein, 2004], Stmn2 [Liu et al., 2002], and Wnt11 [Elizalde et al., 2011]) and cell migration and subsequent development of the central nervous system (Sema6d [Toyofuku et al., 2004], Spock2 [Schnepp et al., 2005], and Spock3 [Yamamoto et al., 2014]). Five of them were also hypermethylated at their TSS 500 and two were not. Treatment with GSK343 did not reactivate the expression of DNA-hypermethylated genes, whereas it promoted re-expression of the two genes that were not DNA methylated (Figure 2E). We showed, by chromatin immunoprecipitation, that the H3K27me3 mark was detected in these 2 genes only in *Sdhb*$^{-/-}$ cells, which returned to baseline following GSK343 treatment (Figures 2F and 2G). In contrast, genes that were DNA hypermethylated in *Sdhb*$^{-/-}$ cells did not bear an increased H3K27me3 mark in *Sdhb*$^{-/-}$ compared with WT cells (Figure S2C), showing that their repression was solely mediated by DNA rather than histone methylation.

To confirm these results with a different PRC2 inhibitor and using a global methylation technique, we used the UNC1999 inhibitor, highly selective for EZH2 and EZH1, and its close analog UNC2400 (>1,000-fold less potent than UNC1999) as a negative control (Figure 2H) and analyzed their effect on methylation profiles using RRBS. Unsupervised hierarchical clustering based on the 1,000 most variant features showed that the methylation profiles of UNC1999-treated cells remained very close to that of UNC2400-treated or untreated cells, regardless of the genotype (Figure 2I). In particular, *Sdhb*$^{-/-}$ imCCs remained hypermethylated when treated with the EZH1/2 inhibitor UNC1999 (Figure 2J).

We have shown previously that *Sdhb*$^{-/-}$ cells display a mesenchymal-like phenotype with increased adhesion and migration properties (Loriot et al., 2015). Notably, PRC2 inhibition did not reduce the migration or adhesion capacities of *Sdhb*$^{-/-}$ cells (Figures 2K and S2D). Altogether, these results suggest that, although PRC2 represses a subset of its targets through deposition of H3K27me3 marks in SDH-deficient cells,

(F and G) Chromatin immunoprecipitation using an antibody against H3K27me3 or negative control rabbit immunoglobulin G (IgG) was performed on the indicated cell lines. The Hand2 (F) and Gdnf (G) genes were quantified by qPCR using primer pairs, as indicated in Figure S7B. Shown is the mean of 3 experiments (+SEM). Student's test was performed to compare the H3K27me3 chromatin immunoprecipitation (ChIP) signal with the background IgG signal.

(H) Inhibition of H3K27me3 by the PRC2 inhibitor UNC1999 compared with vehicle or the negative control UNC2400.

(I) Unsupervised hierarchical clustering based on the 1,000 most variant features in RRBS data from cells treated with UNC1999, UNC2400, or vehicle.

(J) Smooth scatterplot comparing methylation levels identified by RRBS in *Sdhb*$^{-/-}$ cells treated with UNC1999 or vehicle.

(K) Collective migration was followed using a wound scratch assay after treatment with GSK343. Migration is represented as the closure percentage of the wound. The data in (E) and (K) are the mean of 3 independent experiments (+SEM). Student's tests were performed to compare GSK343-treated with untreated cells (*$p < 0.05$, ***$p < 0.001$). Quantification of global 5mC and 5hmC levels in cells treated with GSK343, ChIP-qPCR experiments with additional primer pairs, and adhesion experiments are provided in Figure S2.

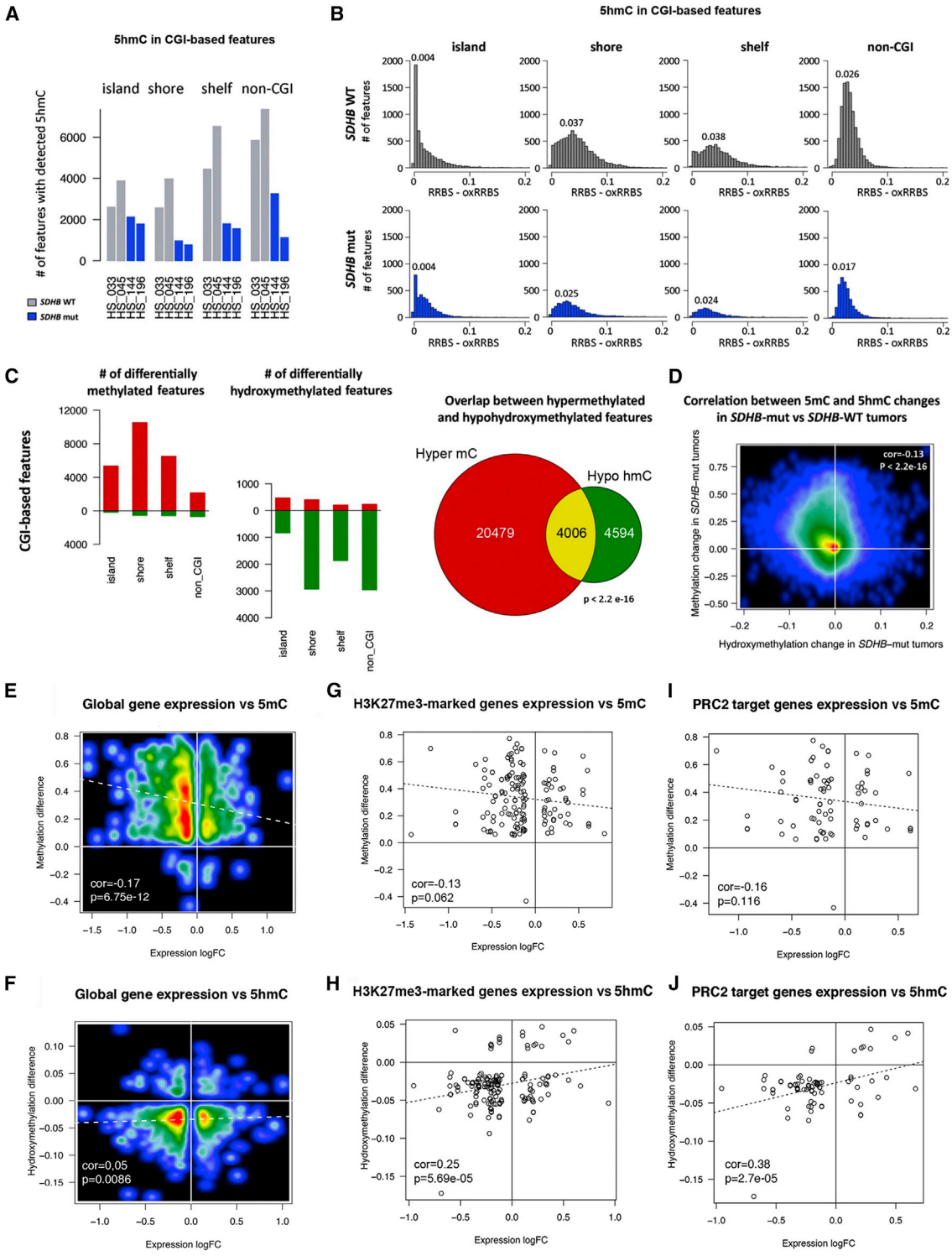


Figure 3. Detection of Methylation or Hydroxymethylation in *SDHB*-mut Compared with *SDHB* Wild-type (WT) Tumors and Correlation between Methylation or Hydroxymethylation Difference and Gene Expression Changes

(A) Number of regions in which 5hmC was detected by (ox)RRBS.

(B) Distribution of 5hmC rates (RRBS-oxRRBS) in regions where it was detected in *SDHB* WT (top) or *SDHB*-mut (bottom) tumors.

(C) Number and overlap of differentially methylated and hydroxymethylated regions in S*DHB*-mut compared with *SDHB*-WT tumors.

(legend continued on next page)

it is not responsible, per se, for the DNA hypermethylation or for the aggressive phenotype of *Sdhb*$^{-/-}$ cells.

Analysis of DNA Hydroxymethylation in SDHB-Deficient Tumors and Cells

Previous studies suggested that DNA hypermethylation could result from succinate-driven inhibition of TET demethylases. To directly test this hypothesis, we precisely quantified 5mC and 5hmC modifications along the genome after enrichment for CpG-rich regions using oxidative RRBS (oxRRBS) (Booth et al., 2012) in human tumors and imCCs. DNA methylation data were highly correlated with meDIP-seq data (Figure S3A) and confirmed the enrichment of PRC2 targets among genes hypermethylated at their TSS 500 in *SDHB*-mut tumors (Benjamini-Hochberg (BH) adjusted p values: BENPORATH_ES_WITH_H3K27ME3 = 1.41E−38; BENPORATH_SUZ12_TARGETS = 1.35E−35; BENPORATH_EED_TARGETS = 5.06E−21; BENPORATH_PRC2_TARGETS = 1.25E−24).

5hmC mapping in tumors from the same genotype was highly correlated, indicating the robustness of the method (Figure S3C). Hydroxymethylation was more abundant in gene bodies than in promoter regions (Figures S3D, S4A, S4B, S5A, and S5B).

Hydroxymethylation was reduced in *SDHB*-mut compared with *SDHB*-WT tumors and cells, sustaining the hypothesis that the hypermethylator phenotype is caused by inhibition of oxidative demethylation. In human tumors, the number of features with detectable 5hmC was reduced by 40% in CGIs, 73% in CGI shores, 69% in CGI shelves, and 67% outside of CGIs (Figure 3A). In terms of gene features, the number of features with detectable 5hmC was reduced by 32% in promoter regions and 54% in gene bodies (Figure S4A). Furthermore, in these features, where 5hmC was detected, the level of hydroxymethylation (RRBS-oxRRBS) was decreased in *SDHB*-mut tumors regardless the feature considered (Figures 3B and S4B). For instance, the peak of the 5hmC rate in gene bodies was 2.9% in *SDHB* WT tumors but only 1.6% in *SDHB*-mut tumors (Figure S4B). Similar results were observed in the cellular model (Figures S5A and S5B).

There was a significant ($p < 2.2e-16$, Fisher's exact test) overlap between 5mC gain and 5hmC loss, with above 4,000 features being both hypermethylated and hypohydroxymethylated (Figures 3C and S4C). We also observed a significant anti-correlation between delta-5mC and delta-5hmC in *SDHB*-mut *versus SDHB* WT tumors, both in CGI-based (Figure 3D) and gene-based features (Figure S4D). Similarly, we found a significant correlation between increased 5mC and decreased 5hmC following *Sdhb* knockout (KO) in cells (Figures S5C and S5D).

As expected, enhanced 5mC levels and reduced 5hmC levels both correlated with a reduction in gene expression (Figures 3E and 3F). Restricting this analysis to PRC2 targets or genes marked by H3K27me3 shows that, as observed in other tumor types (Ohm et al., 2007; Schlesinger et al., 2007), most PRC2 targets were repressed by DNA methylation and not only by histone H3K27 methylation (Figures 3G and 3H). Interestingly, these repressed PRC2 targets also mostly showed low 5hmC levels (Figures 3I and 3J).

Combined Tet1/Tet2 Knockdown Mimics the Methylator Phenotype of Sdhb-Deficient Cells

To evaluate the contribution of TET enzyme inhibition to the hypermethylator phenotype, we knocked down their coding genes in WT imCCs. Because *Tet3* was barely expressed in imCCs (Figure S6A), we generated a double knockdown (KD) by infecting WT imCCs with lentiviruses expressing short hairpin RNAs (shRNAs) targeting *Tet1* and *Tet2*, which led to 50% to 60% inhibition of expression of both enzymes in two different clones (Figure 4A). Global quantification of 5mC and 5hmC by ELISA showed reduced 5hmC and increased 5mC levels in *Tet1*+*Tet2*^{KD} cells, comparable with those observed in *Sdhb*-deficient cells (Figure 4B). RRBS analysis of DNA methylation in shSCR (short hairpin scramble RNA) and *Tet1*+*Tet2*^{KD} imCCs (clone 74) revealed that the hypermethylator phenotypes induced by *Sdhb* KO or *Tet1*+*Tet2*^{KD} were highly similar (Figures 4C and S6B), with a significant overlap of hypermethylated loci at the level of individual CpG sites (Figure 4D) and gene features (Figure S6C; $p < 2.2e-16$, Fisher's exact test). Molecular Signatures Database (MSigDB) enrichment analysis showed strong enrichment in PRC2 targets among the genes hypermethylated at their TSS 500 in *Tet1*+*Tet2*^{KD} cells (Figure S7A), as in *Sdhb*$^{-/-}$ cells. Accordingly, PRC2 targets that are both downregulated and DNA hypermethylated in *Sdhb*$^{-/-}$ cells were also repressed in *Tet1*+*Tet2*^{KD} cells. In contrast, the few targets downregulated but not DNA hypermethylated were only repressed and marked by H3K27me3 in *Sdhb*$^{-/-}$ cells but not in *Tet1*+*Tet2*^{KD} cells (Figures 4E and S7B). Altogether, these data reinforce the demonstration that, in *Sdhb*$^{-/-}$ cells, DNA methylation of most PRC2 targets is the result of TET enzyme inhibition rather than increased PRC2 activity and recruitment of DNA methyltransferase. They are in accordance with other studies in ESCs showing that TET1 and PRC2 have redundant targets (Williams et al., 2011a).

We then investigated the phenotype of *Tet1*+*Tet2*^{KD} imCCs and compared it with *Sdhb*-deficient cells. The proliferation rate of *Tet1*+*Tet2*^{KD} imCCs was lower than that of WT and shSCR cells but slightly higher than that of *Sdhb*$^{-/-}$ cells (Figure 4F). Moreover, *Tet1*+*Tet2*^{KD} imCCs exhibited increased

(D) Correlation between delta-5mC and delta-5hmC in *SDHB*-mut versus *SDHB*-WT tumors. Characteristics of genome-scale mapping of 5mC and 5hmC are provided in Figure S3. 5hmC detection in gene-based features in *SDHB*-mut compared to *SDHB* WT tumors is provided in Figure S4. 5hmC detection in *Sdhb*$^{-/-}$ compared with *Sdhb*-WT imCCs is provided in Figure S5.

(E) Gene expression change versus methylation difference at TSS 500.

(F) Gene expression change versus hydroxymethylation difference at gene bodies.

(G and H) Analysis restricted to gene set "BENPORATH_ES_WITH_H3K27ME3." Shown is gene expression change versus methylation (G) or hydroxymethylation (H) difference at TSS 500.

(I and J) Analysis restricted to gene set "BENPORATH_PRC2_TARGETS." Shown is gene expression change methylation (I) or hydroxymethylation (J) at TSS 500.

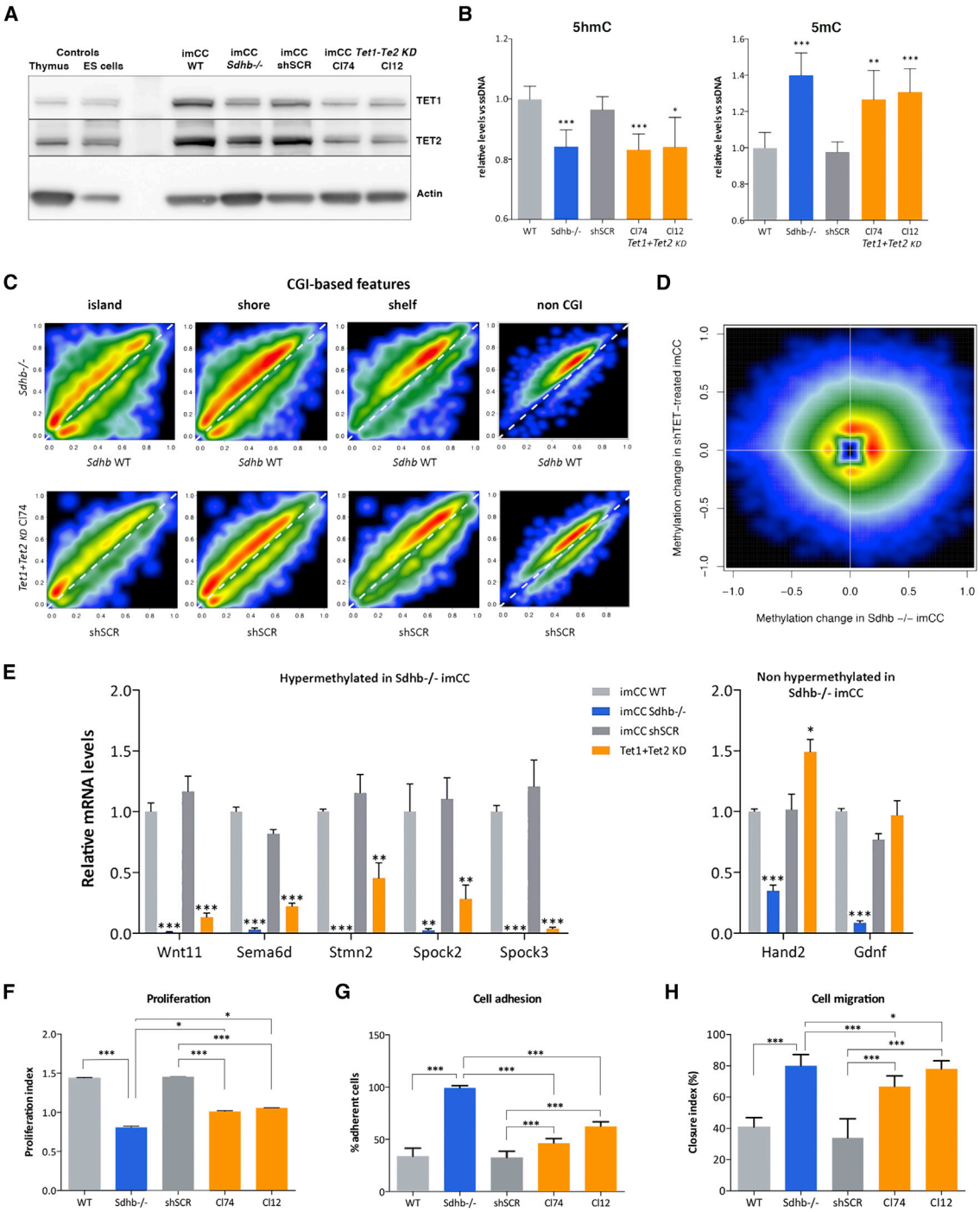


Figure 4. Double Knockdown (KD) of *Tet1* and *Tet2* in Wild-type (WT) imCCs Recapitulates the DNA Hypermethylation Observed in *Sdhb*$^{-/-}$ Cells

(A) Western blot analysis of TET1 and TET2 in total protein extracts from imCCs of the indicated genotypes.

(B) ELISA dosage of global 5hmC (left) and 5mC (right) levels in imCCs infected by scramble shRNA (shSCR) or *Tet1+Tet2* shRNA.

(C) Smooth scatterplot of significantly differentially methylated features (identified by RRBS) in *Sdhb*$^{-/-}$ versus *Sdhb*-WT imCCs (top) or *Tet1+Tet2*^{KD} versus *shSCR* imCCs (bottom) in each kind of CGI-based feature.

(D) Comparison of methylation changes induced by *Tet1+Tet2*^{KD} and *Sdhb*$^{-/-}$ imCCs, considering all differentially methylated CpG sites (delta > 0.1) in at least one condition.

(E) qRT-PCR dosage of known PRC2 targets (hypermethylated or not in *Sdhb*$^{-/-}$ imCCs) in cells of the indicated genotypes.

(F) Proliferation index of the indicated cell lines.

(legend continued on next page)

adhesion and migration compared with WT and shSCR cells but did not reach the levels of adhesion and migration of *Sdhb*$^{-/-}$ cells (Figures 4G and 4H).

DNA Hypermethylation and Hypoxia Act in Synergy to Fully Recapitulate the Sdhb-Deficient Phenotype

Because *Sdhb*$^{-/-}$ cells also exhibit a pseudohypoxic phenotype, we investigated whether hypoxia drives mesenchymal transition in these cells. Pseudohypoxia was characterized by massive overexpression of HIF2α but not HIF1α (Figure 5A). In all cell types, HIF2α stabilization and nuclear translocation can be induced at levels similar to that of *Sdhb*$^{-/-}$ cells by O_2 deprivation for 72 h (Figure 5B). Indeed, cultivating all *Sdhb* WT cells at 2% O_2 induced transient activation of the HIF1α pathway from 4–24 h of hypoxia (as shown by expression of its preferential targets Glut1, Pgk1, and Ldha), whereas the HIF2α pathway (as revealed by Epas1, Mmp9, and Tgfa mRNAs) was induced only after 72 h of hypoxia (Figures 5C and 5D). This is in agreement with transcriptomics analysis in our large cohort of PPGL, which comprised 23 *SDHx*-mutated tumors. We used a list of 11 genes that have been described as HIF1α-specific targets (Figure 5E) and of 9 HIF2α-specific (Figure 5F) targets (Keith et al., 2011) and compared their mean expression in the group of *SDH*-mutated PPGL with *VHL*-, *NF1*-, and *RET*-mutated ones. This analysis showed that SDH- and Von Hippel-Lindau (VHL)-related tumors display a HIF2α signature compared with *RET* or *NF1*-mutated tumors. In contrast, HIF1α targets are highly expressed in VHL-mutated PPGL but not SDH tumors.

In line with previous reports (Thienpont et al., 2016), RRBS and ELISA analyses showed that this modest hypoxia was not sufficient to repress TET activity (Figures 5G and 5H). Indeed, only 1,374 features were differentially methylated between normoxia and hypoxia, whereas over 12,000 were differentially methylated following *Sdhb* KO. These changes were balanced between hyper- and hypomethylation (Figure 5G).

Cultivating cells for 72 h at 2% O_2 mimics the pseudohypoxic features of Sdhb$^{-/-}$ cells. Interestingly, these hypoxic conditions had no or a moderate effect on WT or shSCR cells but enhanced adhesion and migration of *Tet1*+*Tet2*^{KD} imCCs (Figures 6B and 6C). Notably, under these conditions, *Tet1*+*Tet2*^{KD} imCCs reached the migration capacity of *Sdhb* KO cells.

Sdhb$^{-/-}$ cells display a mesenchymal morphology, highlighted by intense staining of actin filaments in all of the cytoplasm, whereas in *Tet1*+*Tet2*^{KD} imCCs, like in WT cells, staining was mainly cortical in normoxia. Strikingly, cultivating *Tet1*+*Tet2*^{KD} imCCs in hypoxia modified their morphology toward an *Sdhb* deficiency-like mesenchymal phenotype (Figure 6D). Accordingly, hypoxic *Tet1*+*Tet2*^{KD} imCCs displayed molecular hallmarks of neuro-endocrine-to-mesenchymal transition, such as Snai1 and Twist1 overexpression and Cdh2 (N-Cadherin is the main cadherin expressed in neuroendocrine cells) downregulation (Figure 6E).

To investigate whether hypoxia could also induce metastatic traits in *Tet1*+*Tet2*^{KD} imCCs *in vivo*, we grew these cells for 72 h in normoxia or hypoxia before injection into the tail vein of immunocompromised mice. This metastatic model has a lung tropism. We therefore sacrificed the mice 41 days after grafting and harvested the lungs, in which the number of metastatic cells was quantified by qPCR on genomic DNA. We showed that the metastatic burden was twice as high in mice injected with hypoxic cells than in those with normoxic cells, confirming *in vivo* the contribution of hypoxia to the metastatic phenotype (Figure 6F).

These data suggest that HIF2α inhibition could counteract metastatic traits of *SDHB*-mut PPGL. To further investigate the effect of HIF2α inhibition on *Sdhb*$^{-/-}$ cells, we silenced HIF2α using specific shRNA lentiviral vectors. To avoid a potential HIF1α response counteracting HIF2α loss, we also infected cells with a lentiviral vector expressing a HIF1α-targeting shRNA together with the shHIF2α (Figures 7A and 7B), and we selected 3 clones bearing only HIF2α or HIF2α+HIF1α silencing. HIF2α inhibition reversed the overexpression of *Mmp9*, *Tgfa*, and *Snai1* observed in *Sdhb* KO cells (Figure 7C). It also had a strong effect on the phenotype of *Sdhb*-deficient cells, leading to changes in cell morphology (Figure 7D) as well as decreased proliferation and migration. In contrast, HIF2α loss had little effect on cell adhesion, in agreement with the small effect of hypoxia on adhesion of Tet-depleted cells (Figures 7E–7G). HIF1α repression had no additional effect on all of these features.

Altogether, our data demonstrate that hypermethylation and repression of PRC2 targets and developmental genes increase phenotypic plasticity, allowing acquisition of mesenchymal traits induced by HIF2α to recapitulate the SDHB deficiency phenotype.

DISCUSSION

In this study, we investigated the mechanisms by which hypermethylation occurs in SDH-deficient tumors and cells. Because of the low levels of 5hmC in tumors and cultured somatic cells, there have been very few studies that analyzed the content and distribution of 5hmC in non-embryonic cells and cancer. Hence, the link between SDH tumor hypermethylation and TET inhibition has been postulated but actually never truly demonstrated. Our data show that SDH-driven hypermethylation does result from TET inhibition and subsequent loss of 5hmC.

It may seem contradictory that the hypermethylator phenotype of SDH-deficient tumors mainly affects CGIs, whereas hypo-hydroxymethylation is mostly observed in gene bodies. However, it is important to note that hypo-hydroxymethylation in CGIs is very difficult to detect because of the very low level of 5hmC in these features (about 0.4% in our data). Because of this very low level at baseline, we are

(G) Adhesion of the indicated cell lines 3 h after plating.
(H) Closure index of the wound scratch assay after 15-h migration of the indicated cell lines.
The data in (B), (E), (F), (G) and (H) are the mean of 3 experiments (+SEM). Student's test was performed to compare *Sdhb*$^{-/-}$ cells with WT cells and *Tet1*+*Tet2*^{KD} cells with shSCR cells and *Sdhb*$^{-/-}$ cells (*p < 0.05, **p < 0.01, ***p < 0.001). TET3 protein levels and RRBS analyses for each kind of gene-based features are provided in Figure S6.

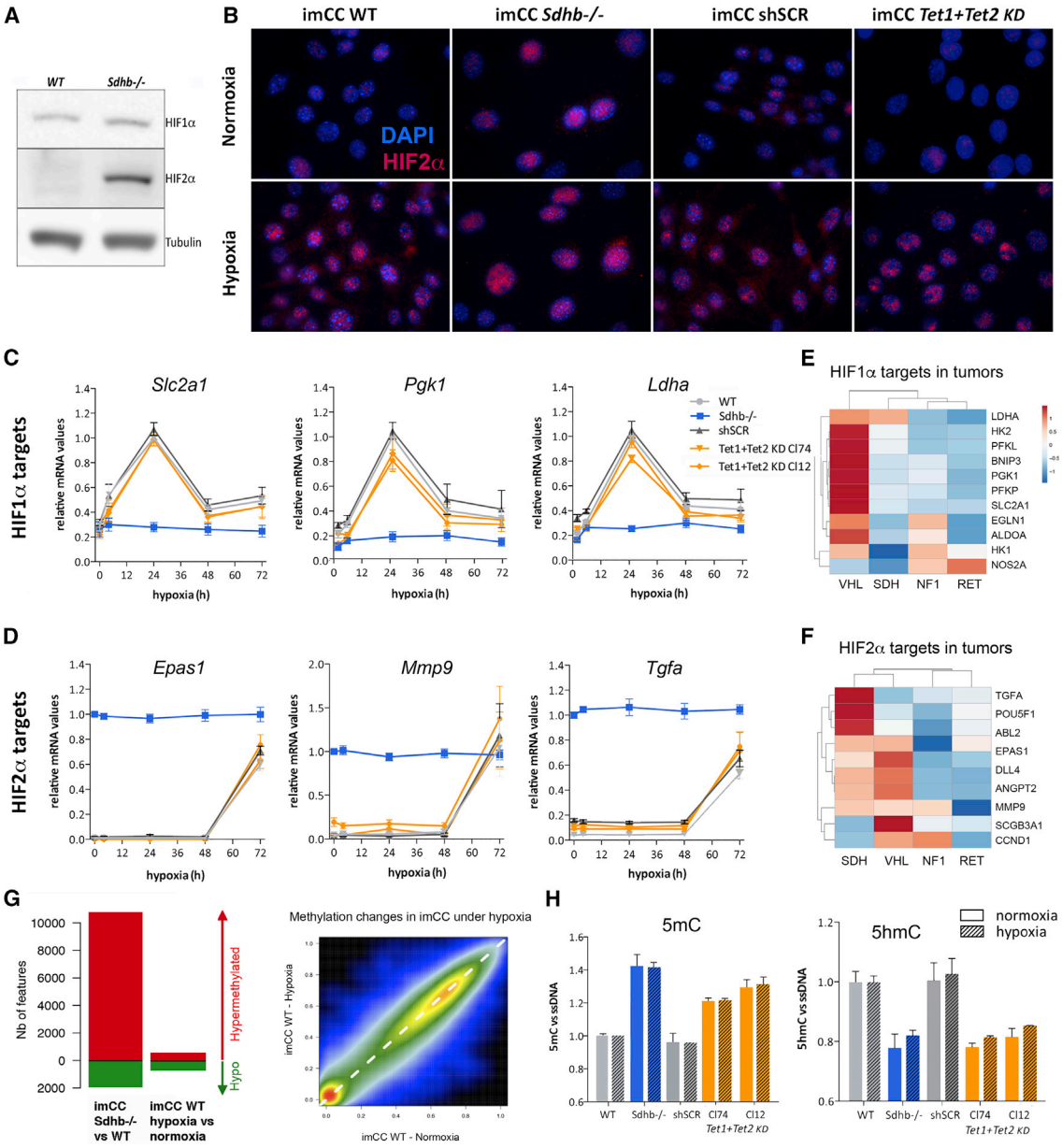


Figure 5. Pseudohypoxia in *Sdhb*$^{-/-}$ imCCs Leads to Stabilization of HIF2α and Can Be Mimicked by Long-Term Moderate Hypoxia

(A) Western blot of HIF1α and HIF2α in total cellular extracts of WT or *Sdhb*$^{-/-}$ imCCs cultured in normoxia (21% O_2).

(B) HIF2α immunofluorescence staining in cells cultivated in normoxia or hypoxia (2% O_2) for 72 h.

(C and D) Kinetics of induction of various (C) HIF1α or (D) HIF2α targets by qRT-PCR measurements in the indicated cell lines cultured at 2% O_2 in a hypoxic chamber.

(E and F) Heatmap based on mean expression of (E) HIF1α or (F) HIF2α target genes in human PPGL with *SDH* (n = 23), *VHL* (n = 40), *NF1* (n = 37), or *RET* (n = 19) driver mutations.

(G) Left: number of differentially methylated features in *Sdhb*$^{-/-}$ (versus WT) or hypoxic (versus normoxic) imCCs. Right: smooth scatterplot of methylation levels identified by RRBS in hypoxic compared with normoxic WT imCCs.

(H) Global 5hmC and 5mC levels, measured by ELISA in cells incubated for 72 h at 21% or 2% O_2. Student's test was performed to compare normoxic and hypoxic conditions for 5hmC and 5mC quantification. No significant difference was observed.

The data in (C), (D) and (H) are the mean of 3 experiments (+ SEM).

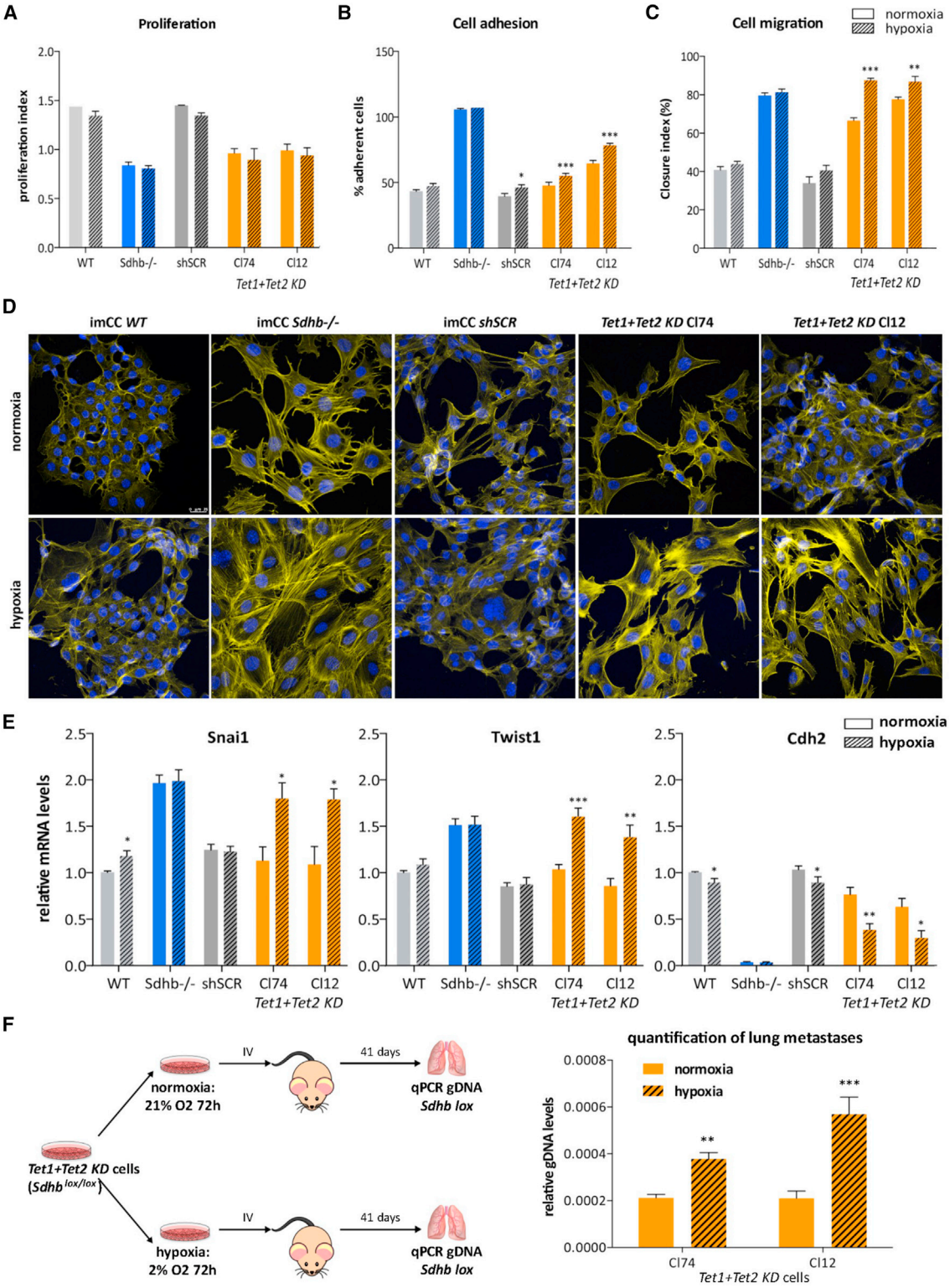


Figure 6. Hypoxia Synergizes with TET Inhibition to Drive Neuro-endocrine-to-Mesenchymal Transition and Subsequent Metastatic Traits

(A) The indicated cell lines were cultivated for 72 h at 21% (normoxia) or 2% O_2 (hypoxia) before running a 7 day proliferation test in normoxia or hypoxia.

(B) After 72 h of incubation at 21% or 2% O_2, the indicated cell lines were plated in normoxia or hypoxia, and the percentage of adherent cells was quantified 3 h later.

(legend continued on next page)

underpowered to detect a decrease of 5hmC within a single CGI. However, we detect 5hmC in a lower number of CGIs in SDH-mut compared with SDH WT tumors (Figure 3B). Thus, 5hmC decreases in CGIs following SDH deficiency, even though this phenomenon is hard to quantify at the level of a single island. The correlation between the intensity of 5mC and 5hmC changes (Figure 3D) is also a strong argument for the pairing of these two changes.

We reveal that a significant fraction of genes hypermethylated consecutive to *SDHB* mutation are known PRC2 targets and genes marked by H3K27me3 histone modification in ESCs. Polycomb groups are mainly involved in transient repression of developmental genes in ESCs through deposition of the H3K27me3 mark at bivalent promoters. Strikingly, several studies have shown that polycomb targets are more prone (up to 12-fold) to cancer-specific hypermethylation (Ohm et al., 2007; Schlesinger et al., 2007) in cancers not driven by oncometabolites, supporting a stem cell origin of cancer in which reversible gene repression would be replaced by permanent silencing. This switch would not cause *de novo* repression but might significantly reduce epigenetic plasticity, locking the cell into a perpetual state of self-renewal and predisposing it to subsequent malignant transformation. The fact that polycomb targets are not highly methylated in non-SDH PPGL suggests a different oncogenic origin in these mostly benign tumors. Thus, our results are in accordance with studies showing that underexpression of polycomb-regulated genes is restricted to poorly differentiated tumors and associated with poor clinical outcome (Ben-Porath et al., 2008).

Because two PRC2 core components, EZH2 and SUZ12, are overexpressed in SDH-deficient tumors, we investigated whether hypermethylation of these gene sets was caused by PRC2 activity. Although a subset of PRC2 targets are indeed repressed by PRC2-mediated trimethylation of H3K27, PRC2 pharmacological inhibition does not counteract DNA hypermethylation in *Sdhb*$^{-/-}$ cells, and *Tet1*+*Tet2*^{KD} imCCs also show DNA hypermethylation, preferentially at PRC2 targets. This points to a prominent role of oncometabolite-mediated inhibition of TET enzymes rather than the DNA methyltransferases DNMT1 and DNMT3a recruited by PRC2.

Several studies have shown redundancy between PRC2 and TET targets in ESCs (Pastor et al., 2011; Verma et al., 2018; Williams et al., 2011a; Wu et al., 2011). Neri et al. (2013) showed a physical interaction between TET1 and the PRC2 complex specifically in ESCs, whereas Williams et al. (2011a) failed to find this interaction in HEK293 cells. It thus remains unclear whether TET enzymes still convert 5mC to 5hmC at PRC2 targets in differentiated cells and in cancer cells. Redundancy between TET and PRC2 targets in cancer cells has been demonstrated by some studies (Putiri et al., 2014; Thomson et al., 2016) but denied by others (Fernandez et al., 2018; Uribe-Lewis et al., 2015). Our study differs in that we did not compare normal with cancer tissues, but we compared tumor samples carrying or not carrying *SDHB* mutations and isogenic cells carrying or not carrying *Sdhb* deletion or *Tet1*+*Tet2* KD. Under these conditions, we were able to demonstrate that, in PPGL tumors and in mouse cells originating from the adrenal medulla, TET enzymes counteract DNA methylation preferentially at genes marked by H3K27me3 and targeted by PRC2 in ESCs. Thus, TET inhibition leads to repression of PRC2 target genes notably involved in neural differentiation (*Stmn2* [Liu et al., 2002] and *Wnt11* [Elizalde et al., 2011]) and cell migration and subsequent development of the central nervous system (*Sema6d* [Toyofuku et al., 2004], *Spock2* [Schnepp et al., 2005], and *Spock3* [Yamamoto et al., 2014]).

Mechanistic insights into the PRC2-TET relationship could be gained from the literature on *WT1* mutations in acute myeloid leukemia (AML), which are mutually exclusive with *IDH1/2, TET2* (Wang et al., 2015), and *EZH2* (Bolouri et al., 2018) mutations. Interestingly, WT1 can recruit EZH2 (Xu et al., 2011), TET2 (Wang et al., 2015), (Rampal et al., 2014) and TET3 (Rampal et al., 2014) to specific targets and may therefore be the clue to explain the redundancy between PRC2 and TET targets. Accordingly, Sinha et al. (2015) showed that *WT1* mutations lead to hypermethylation of PRC2 targets in AML. However, WT1 is hardly expressed in PPGL cells and imCCs (data not shown), so another, still unknown transcription factor and/or non-coding RNA is probably involved in recruiting TET enzymes at PRC2 target promoters in PPGL.

In the second part of this study, we analyzed the functional consequences of DNA hypermethylation because of TET silencing and HIF2α stabilization. We show that the mesenchymal-like phenotype and metastatic behavior of *Sdhb*-deficient cells result from synergistic effects of TET inhibition and pseudohypoxia. Her et al. (2015) showed that TET inhibition by succinate is oxygen dependent in SDH loss models of PPGL. They suggested that the increased incidence and worst prognosis of SDH-related PPGL in patients living at high altitude or with chronic hypoxia because of respiratory or circulatory pathologies is due to TET inhibition by hypoxia. In contrast, we showed previously, in a large cohort of PPGL from patients living at normal altitude, that DNA hypermethylation was evidenced in all SDH-mutated PPGL (Letouzé et al., 2013). Similarly, *Sdhb* KO in imCCs results in TET-mediated DNA hypermethylation even under normoxic conditions. The hypoxic conditions we used in this study were neither

(C) Closure index of the wound scratch assay after 15-h migration of the indicated cell lines pre-cultured for 72 h at 21% or 2% O_2.
(D) Actin staining was performed using fluorescent phalloidin toxin in the indicated cell lines cultivated for 72 h at 21% or 2% O_2.
(E) qRT-PCR measurement of known drivers of neuro-endocrine-to-mesenchymal transition (Loriot et al., 2015) in the indicated cell lines incubated for 72 h at 21% or 2% O_2. All data are the mean of 3 experiments.
(F) Evaluation of *in vivo* metastatic behavior of *Tet1*+*Tet2* KD imCCs (Cl74 and Cl12) precultured for 72 h at 21% or 2% O_2. After preculture in normoxia or hypoxia, 10^6 cells were injected in PBS in the tail vein of NMRI nude mice. 41 days later, the mice were sacrificed, and the lungs were snap frozen in liquid nitrogen. genomic DNA (gDNA) extraction was performed on entire lungs, and metastatic charge was quantified by qPCR using primers specific for the loxP site present in imCCs. The data in (A), (B), (C) and (E) are the mean of 3 experiments (+ SEM). Student's test was performed to compare normoxic and hypoxic conditions (*$p < 0.05$, **$p < 0.01$, ***$p < 0.001$).

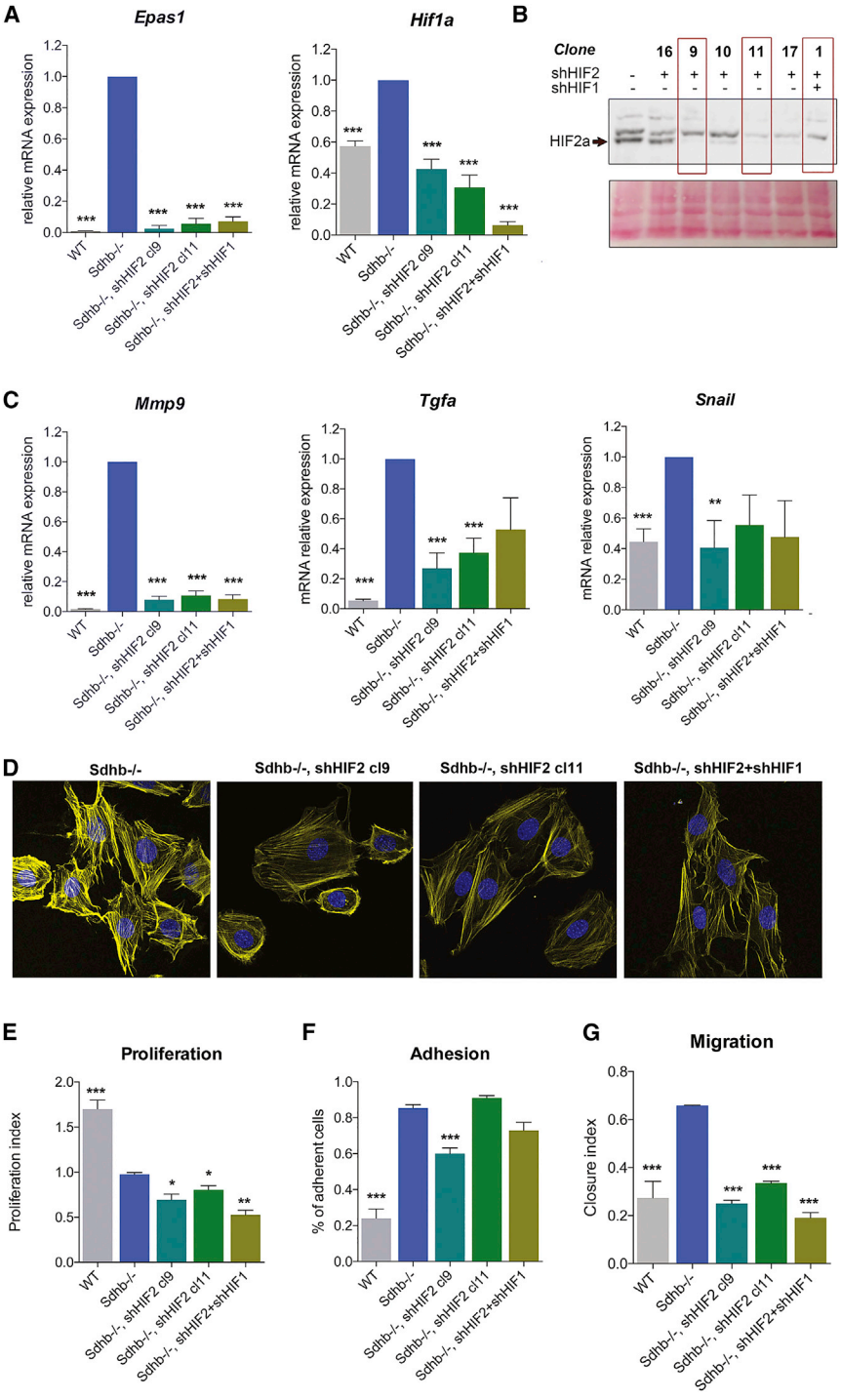


Figure 7. HIF2α Silencing Counteracts Pseudohypoxia in *Sdhb*$^{-/-}$ Cells and Reverses Their Mesenchymal Phenotype

(A) qRT-PCR measurement of *Epas1* and *Hif1α* expression in the indicated cell lines and clones.

(B) Protein expression of Hif2α in pure clones of *Sdhb*$^{-/-}$ imCCs stably expression shRNAs targeting Hif2α (clones 16, 9, 10, 11, and 17) or HIF2α and HIF1α (clone 1). Clones 9, 11, and 1 had nearly complete extinction of Hif2α expression and were selected for further experiments.

(C) qRT-PCR measurement of *Mmp9* and *Tgfa* (markers of pseudohypoxia) and *Snai1* (EMT marker) expression in the indicated cell lines and clones.

(D) Actin staining was performed using fluorescent phalloidin toxin in the indicated cell lines and clones.

(E) Proliferation index of the indicated cell lines and clones.

(F) Adhesion of the indicated cell lines 1 h after plating.

(G) Closure index of the wound scratch assay after 10-h migration of the indicated cell lines.

The data in (A), (C), (E), (F), and (G) are the mean of 3 experiments (+ SEM). Student's test was performed to compare all cell lines with *Sdhb*$^{-/-}$ cells (*p < 0.05, **p < 0.01, ***p < 0.001).

necessary nor sufficient to inhibit TET activity in our cells. Therefore, the effect of hypoxia we observed on cell behavior is not mediated by increased DNA methylation but, rather, by HIF2α-mediated gene transcription. Thienpont et al. (2016) showed that acute hypoxia is necessary to repress TET activity because the Michaelis Constant (Km) for TET1 and TET2 were, respectively, 0.31% and 0.53% O_2. Thus, altitude may synergize with oncometabolites and intra-tumoral acute hypoxia in repression of TET enzymes, but it is probably not the leading mechanism.

HIF1α and HIF2α proteins have been found to be overexpressed in the nuclei of some SDH-deficient tumors, but a few studies suggest that HIF2α plays a more important role than HIF1α in tumorigenesis (Favier et al., 2009; Holmquist-Mengelbier et al., 2006; Nilsson et al., 2005; Qin et al., 2014). Here we demonstrate that pseudohypoxia in *Sdhb*$^{-/-}$ and in SDH-mutated PPGL is driven by HIF2α stabilization rather than HIF1α and that the kinetics of stabilization of both proteins may explain this observation. Indeed, HIF1α is stabilized in short-term acute hypoxia, whereas HIF2α is stabilized in moderate but prolonged hypoxia (Holmquist-Mengelbier et al., 2006; Uchida et al., 2004). We confirmed previous observations that HIF1α levels decline after several hours of hypoxia (Koh et al., 2011; Uchida et al., 2004), whereas HIF2α levels increase later in long-term hypoxia (Holmquist-Mengelbier et al., 2006; Uchida et al., 2004). Several mechanisms may play a role in HIF1α decline in long-term hypoxia: HIF-mediated expression of antisense transcripts from the *HIF1A* locus (Uchida et al., 2004); HAF-, HSP70-, or Carboxyl terminus of HSC70-interacting protein (CHIP)-mediated HIF1α-specific degradation (Koh

et al., 2008, 2011; Luo et al., 2010). Thus, pseudohypoxia mimics long-term hypoxia with massive HIF2α stabilization but no HIF1α stabilization.

High HIF2α levels have been implicated in the undifferentiated and aggressive phenotype of some pseudohypoxic cancers (Myszczyszyn et al., 2015; Pietras et al., 2010). Here we show that, in chromaffin cells, hypoxia is not sufficient to induce EMT but synergizes with epigenetic modifications resulting from SDHB loss to drive neuro-endocrine-to-mesenchymal transition and subsequent invasive behavior. This may explain why pseudohypoxic *VHL*-mutated PPGL (which are not highly hypermethylated) are rarely metastatic, whereas *SDHB*-mut PPGL are more prone to metastasis.

Similarly, all oncometabolites do not identically repress the various 2-OG-dependant dioxygenases, which could be a clue regarding the different phenotypes of oncometabolite-mediated tumors. Indeed, histone demethylases such as JMJD2A are inhibited by all oncometabolites (Chowdhury et al., 2011; Xiao et al., 2012), with higher affinity for 2-hydroxyglutarate (2-HG) than for succinate and fumarate, whereas the affinity of TET enzymes for 2-HG is lower than for succinate and fumarate (Laukka et al., 2016). Finally, PHDs are inhibited by succinate and fumarate (Isaacs et al., 2005; Selak et al., 2005), but the effect of the R-enantiomer of 2-hydroxylglutarate (R-2-HG) is still debated (Chowdhury et al., 2011; Williams et al., 2011b; Zhao et al., 2009) and may even activate these enzymes (Koivunen et al., 2012; Losman et al., 2013). In consequence, *IDH*-mutated gliomas, which have a good prognosis, would be hypermethylated but not pseudohypoxic. Conversely, SDH and FH tumors, which are both pseudohypoxic and DNA hypermethylated, are associated with increased risk of regional and distant spread in PPGL as well as hereditary leiomyomatosis and renal cell cancer (caused by germline *FH* mutations). Thus, the comparison of the distinct metastatic susceptibility of VHL, IDH, and FH tumors (Henegan and Gomez, 2016) is in accordance with our data showing that TET inhibition and pseudohypoxia are needed to synergistically drive malignancy.

We show that, surprisingly, cell adhesion was very high in $Sdhb^{-/-}$ cells compared with WT or $Tet1{+}Tet2^{KD}$ cells but was not highly affected by HIF2α inhibition or hypoxia. This suggests that the remarkably high adhesion properties of $Sdhb^{-/-}$ cells may be in great part driven by pathways other than DNA methylation and pseudohypoxia; for example, metabolic reprogramming (Lussey-Lepoutre et al., 2015; Sousa et al., 2019).

Although these findings do not explain why only half of all *SDHB*-mut tumors become metastatic, we and others have shown recently that *TERT* activation and *ATRX* mutations are frequently associated with metastatic progression of these tumors (Fishbein et al., 2015; Svahn et al., 2018; Dwight et al., 2018; Job et al., 2019). Nonetheless, it should be noted that imCCs have achieved spontaneous immortalization right before *Sdhb* inactivation (Letouzé et al., 2013). Thus, we propose a tripartite model where TET-mediated hypermethylation, pseudohypoxia, and immortalization propel the transition of *SDHB*-mut tumors toward metastasis.

STAR★METHODS

Detailed methods are provided in the online version of this paper and include the following:

- KEY RESOURCES TABLE
- LEAD CONTACT AND MATERIALS AVAILABILITY
- EXPERIMENTAL MODEL AND SUBJECT DETAILS
  - Patients and tumor samples
  - Mammalian cell line
  - Data generated
  - Mouse model
- METHOD DETAILS
  - MeDIP-seq analysis
  - RNA-seq analysis
  - oxRRBS and RRBS Analyses
  - 5hmC detection using (ox)RRBS data
  - Differential (hydroxy)methylation analysis
  - Gene set enrichment analysis
  - Inhibition of PRC2 activity
  - Proliferation assay
  - Adhesion assay
  - Wound scratch assay
  - shRNA stable transduction
  - Reversed Transcription and Quantitative Real-Time PCR
  - ChIP-qPCR
  - 5mC and 5hmC ELISA
  - Western Blot analysis
  - Fluorescent staining
  - *In vivo* metastasis assay
- QUANTIFICATION AND STATISTICAL ANALYSIS
- DATA AND CODE AVAILABILITY

SUPPLEMENTAL INFORMATION

Supplemental Information can be found online at https://doi.org/10.1016/j.celrep.2020.03.022.

ACKNOWLEDGMENTS

We thank Charles Marcaillou, Sylvain Guibert, and Céline Vallot for technical contributions and advice and Catherine Tritscher for precious administrative help. This work has received funding from the European Union (FP7/2007-2013 no. 259735), The Plan Cancer, Epigénétique et Cancer (EPIG201303 METABEPIC), The Paradifference Foundation, and the Cancer Research for Personalized Medicine (CARPEM) project (Site de Recherche Intégré sur le Cancer [SIRIC]). We thank all members of the Genetics Department, Biological Resources Center and Tumor Bank Platform, Hôpital Européen Georges Pompidou (BB-0033-00063). This work is part of the "Cartes d'Identité des Tumeurs (CIT) program" funded and developed by the Ligue Nationale contre le Cancer. S.M. is the recipient of a fellowship from La Fondation pour la Recherche Médicale. J.G. is the recipient of a fellowship from La Ligue Nationale contre le Cancer.

AUTHOR CONTRIBUTIONS

A.M. contributed to acquisition, analysis, and interpretation of data; management of the project; and preparation and writing of the manuscript. J.G., S.M., A.B., M.-J.F., and J.W. contributed to acquisition of data. L.-J.C.-V. contributed to the acquisition and analysis of data. S.J. contributed to analysis of transcriptomics data. A.-P.G.-R. contributed to management of the project. E.L.

contributed to conception of the study, analysis of sequencing data, and preparation and revision of the manuscript. J.F. contributed to conception of the study, management of the project, analysis and interpretation of data, and preparation and revision of the manuscript.

DECLARATION OF INTERESTS

The authors declare no competing interests.

Received: February 6, 2019
Revised: January 24, 2020
Accepted: March 6, 2020
Published: March 31, 2020

REFERENCES

Akalin, A., Kormaksson, M., Li, S., Garrett-Bakelman, F.E., Figueroa, M.E., Melnick, A., and Mason, C.E. (2012). methylKit: a comprehensive R package for the analysis of genome-wide DNA methylation profiles. Genome Biol. *13*, R87.

Amar, L., Baudin, E., Burnichon, N., Peyrard, S., Silvera, S., Bertherat, J., Bertagna, X., Schlumberger, M., Jeunemaitre, X., Gimenez-Roqueplo, A.P., and Plouin, P.F. (2007). Succinate dehydrogenase B gene mutations predict survival in patients with malignant pheochromocytomas or paragangliomas. J. Clin. Endocrinol. Metab. *92*, 3822–3828.

Anders, S., and Huber, W. (2010). Differential expression analysis for sequence count data. Genome Biol. *11*, R106.

Anders, S., Pyl, P.T., and Huber, W. (2015). HTSeq–a Python framework to work with high-throughput sequencing data. Bioinformatics *31*, 166–169.

Ben-Porath, I., Thomson, M.W., Carey, V.J., Ge, R., Bell, G.W., Regev, A., and Weinberg, R.A. (2008). An embryonic stem cell-like gene expression signature in poorly differentiated aggressive human tumors. Nat. Genet. *40*, 499–507.

Bolouri, H., Farrar, J.E., Triche, T., Jr., Ries, R.E., Lim, E.L., Alonzo, T.A., Ma, Y., Moore, R., Mungall, A.J., Marra, M.A., et al. (2018). The molecular landscape of pediatric acute myeloid leukemia reveals recurrent structural alterations and age-specific mutational interactions. Nat. Med. *24*, 103–112.

Booth, M.J., Branco, M.R., Ficz, G., Oxley, D., Krueger, F., Reik, W., and Balasubramanian, S. (2012). Quantitative sequencing of 5-methylcytosine and 5-hydroxymethylcytosine at single-base resolution. Science *336*, 934–937.

Burnichon, N., Vescovo, L., Amar, L., Libé, R., de Reynies, A., Venisse, A., Jouanno, E., Laurendeau, I., Parfait, B., Bertherat, J., et al. (2011). Integrative genomic analysis reveals somatic mutations in pheochromocytoma and paraganglioma. Hum. Mol. Genet. *20*, 3974–3985.

Castro-Vega, L.J., Buffet, A., De Cubas, A.A., Cascón, A., Menara, M., Khalifa, E., Amar, L., Azriel, S., Bourdeau, I., Chabre, O., et al. (2014). Germline mutations in FH confer predisposition to malignant pheochromocytomas and paragangliomas. Hum. Mol. Genet. *23*, 2440–2446.

Chowdhury, R., Yeoh, K.K., Tian, Y.M., Hillringhaus, L., Bagg, E.A., Rose, N.R., Leung, I.K., Li, X.S., Woon, E.C., Yang, M., et al. (2011). The oncometabolite 2-hydroxyglutarate inhibits histone lysine demethylases. EMBO Rep. *12*, 463–469.

Clark, G.R., Sciacovelli, M., Gaude, E., Walsh, D.M., Kirby, G., Simpson, M.A., Trembath, R.C., Berg, J.N., Woodward, E.R., Kinning, E., et al. (2014). Germline FH mutations presenting with pheochromocytoma. J. Clin. Endocrinol. Metab. *99*, E2046–E2050.

Dwight, T., Flynn, A., Amarasinghe, K., Benn, D.E., Lupat, R., Li, J., Cameron, D.L., Hogg, A., Balachander, S., Candiloro, I.L.M., et al. (2018). *TERT* structural rearrangements in metastatic pheochromocytomas. Endocr. Relat. Cancer *25*, 1–9.

Elizalde, C., Campa, V.M., Caro, M., Schlangen, K., Aransay, A.M., Vivanco, Md., and Kypta, R.M. (2011). Distinct roles for Wnt-4 and Wnt-11 during retinoic acid-induced neuronal differentiation. Stem Cells *29*, 141–153.

Favier, J., Brière, J.J., Burnichon, N., Rivière, J., Vescovo, L., Benit, P., Giscos-Douriez, I., De Reyniès, A., Bertherat, J., Badoual, C., et al. (2009). The Warburg effect is genetically determined in inherited pheochromocytomas. PLoS ONE *4*, e7094.

Fernandez, A.F., Bayón, G.F., Sierra, M.I., Urdinguio, R.G., Toraño, E.G., García, M.G., Carella, A., López, V., Santamarina, P., Pérez, R.F., et al. (2018). Loss of 5hmC identifies a new type of aberrant DNA hypermethylation in glioma. Hum. Mol. Genet. *27*, 3046–3059.

Figueroa, M.E., Abdel-Wahab, O., Lu, C., Ward, P.S., Patel, J., Shih, A., Li, Y., Bhagwat, N., Vasanthakumar, A., Fernandez, H.F., et al. (2010). Leukemic IDH1 and IDH2 mutations result in a hypermethylation phenotype, disrupt TET2 function, and impair hematopoietic differentiation. Cancer Cell *18*, 553–567.

Fishbein, L., Khare, S., Wubbenhorst, B., DeSloover, D., D'Andrea, K., Merrill, S., Cho, N.W., Greenberg, R.A., Else, T., Montone, K., et al. (2015). Whole-exome sequencing identifies somatic ATRX mutations in pheochromocytomas and paragangliomas. Nat. Commun. *6*, 6140.

Gimenez-Roqueplo, A.P., Favier, J., Rustin, P., Rieubland, C., Crespin, M., Nau, V., Khau Van Kien, P., Corvol, P., Plouin, P.F., and Jeunemaitre, X.; COMETE Network (2003). Mutations in the SDHB gene are associated with extra-adrenal and/or malignant phaeochromocytomas. Cancer Res. *63*, 5615–5621.

Guo, W., Fiziev, P., Yan, W., Cokus, S., Sun, X., Zhang, M.Q., Chen, P.Y., and Pellegrini, M. (2013). BS-Seeker2: a versatile aligning pipeline for bisulfite sequencing data. BMC Genomics *14*, 774.

Haffner, M.C., Pellakuru, L.G., Ghosh, S., Lotan, T.L., Nelson, W.G., De Marzo, A.M., and Yegnasubramanian, S. (2013). Tight correlation of 5-hydroxymethylcytosine and Polycomb marks in health and disease. Cell Cycle *12*, 1835–1841.

Heger, A., Webber, C., Goodson, M., Ponting, C.P., and Lunter, G. (2013). GAT: a simulation framework for testing the association of genomic intervals. Bioinformatics *29*, 2046–2048.

Henegan, J.C., Jr., and Gomez, C.R. (2016). Heritable Cancer Syndromes Related to the Hypoxia Pathway. Front. Oncol. *6*, 68.

Her, Y.F., Nelson-Holte, M., and Maher, L.J., 3rd. (2015). Oxygen concentration controls epigenetic effects in models of familial paraganglioma. PLoS ONE *10*, e0127471.

Holmquist-Mengelbier, L., Fredlund, E., Löfstedt, T., Noguera, R., Navarro, S., Nilsson, H., Pietras, A., Vallon-Christersson, J., Borg, A., Gradin, K., et al. (2006). Recruitment of HIF-1alpha and HIF-2alpha to common target genes is differentially regulated in neuroblastoma: HIF-2alpha promotes an aggressive phenotype. Cancer Cell *10*, 413–423.

Isaacs, J.S., Jung, Y.J., Mole, D.R., Lee, S., Torres-Cabala, C., Chung, Y.L., Merino, M., Trepel, J., Zbar, B., Toro, J., et al. (2005). HIF overexpression correlates with biallelic loss of fumarate hydratase in renal cancer: novel role of fumarate in regulation of HIF stability. Cancer Cell *8*, 143–153.

Job, S., Draskovic, I., Burnichon, N., Buffet, A., Cros, J., Lépine, C., Venisse, A., Robidel, E., Verkarre, V., Meatchi, T., et al. (2019). Telomerase activation and ATRX mutations are independent risk factors for metastatic pheochromocytoma and paraganglioma. Clin. Cancer Res. *25*, 760–770.

Keith, B., Johnson, R.S., and Simon, M.C. (2011). HIF1α and HIF2α: sibling rivalry in hypoxic tumour growth and progression. Nat. Rev. Cancer *12*, 9–22.

Killian, J.K., Kim, S.Y., Miettinen, M., Smith, C., Merino, M., Tsokos, M., Quezado, M., Smith, W.I., Jr., Jahromi, M.S., Xekouki, P., et al. (2013). Succinate dehydrogenase mutation underlies global epigenomic divergence in gastrointestinal stromal tumor. Cancer Discov. *3*, 648–657.

Kim, D., Pertea, G., Trapnell, C., Pimentel, H., Kelley, R., and Salzberg, S.L. (2013). TopHat2: accurate alignment of transcriptomes in the presence of insertions, deletions and gene fusions. Genome Biol. *14*, R36.

Koh, M.Y., Darnay, B.G., and Powis, G. (2008). Hypoxia-associated factor, a novel E3-ubiquitin ligase, binds and ubiquitinates hypoxia-inducible factor 1alpha, leading to its oxygen-independent degradation. Mol. Cell. Biol. *28*, 7081–7095.

Koh, M.Y., Lemos, R., Jr., Liu, X., and Powis, G. (2011). The hypoxia-associated factor switches cells from HIF-1α- to HIF-2α-dependent signaling

promoting stem cell characteristics, aggressive tumor growth and invasion. Cancer Res. *71*, 4015–4027.

Koivunen, P., Lee, S., Duncan, C.G., Lopez, G., Lu, G., Ramkissoon, S., Losman, J.A., Joensuu, P., Bergmann, U., Gross, S., et al. (2012). Transformation by the (R)-enantiomer of 2-hydroxyglutarate linked to EGLN activation. Nature *483*, 484–488.

Konze, K.D., Ma, A., Li, F., Barsyte-Lovejoy, D., Parton, T., Macnevin, C.J., Liu, F., Gao, C., Huang, X.P., Kuznetsova, E., et al. (2013). An orally bioavailable chemical probe of the Lysine Methyltransferases EZH2 and EZH1. ACS Chem. Biol. *8*, 1324–1334.

Langmead, B., and Salzberg, S.L. (2012). Fast gapped-read alignment with Bowtie 2. Nat. Methods *9*, 357–359.

Laukka, T., Mariani, C.J., Ihantola, T., Cao, J.Z., Hokkanen, J., Kaelin, W.G., Jr., Godley, L.A., and Koivunen, P. (2016). Fumarate and Succinate Regulate Expression of Hypoxia-inducible Genes via TET Enzymes. J. Biol. Chem. *291*, 4256–4265.

Lee, T.I., Jenner, R.G., Boyer, L.A., Guenther, M.G., Levine, S.S., Kumar, R.M., Chevalier, B., Johnstone, S.E., Cole, M.F., Isono, K., et al. (2006). Control of developmental regulators by Polycomb in human embryonic stem cells. Cell *125*, 301–313.

Letouzé, E., Martinelli, C., Loriot, C., Burnichon, N., Abermil, N., Ottolenghi, C., Janin, M., Menara, M., Nguyen, A.T., Benit, P., et al. (2013). SDH mutations establish a hypermethylator phenotype in paraganglioma. Cancer Cell *23*, 739–752.

Li, H., Handsaker, B., Wysoker, A., Fennell, T., Ruan, J., Homer, N., Marth, G., Abecasis, G., and Durbin, R.; 1000 Genome Project Data Processing Subgroup (2009). The Sequence Alignment/Map format and SAMtools. Bioinformatics *25*, 2078–2079.

Liu, Z., Chatterjee, T.K., and Fisher, R.A. (2002). RGS6 interacts with SCG10 and promotes neuronal differentiation. Role of the G gamma subunit-like (GGL) domain of RGS6. J. Biol. Chem. *277*, 37832–37839.

Loriot, C., Domingues, M., Berger, A., Menara, M., Ruel, M., Morin, A., Castro-Vega, L.J., Letouzé, É., Martinelli, C., Bemelmans, A.P., et al. (2015). Deciphering the molecular basis of invasiveness in Sdhb-deficient cells. Oncotarget *6*, 32955–32965.

Losman, J.A., Looper, R.E., Koivunen, P., Lee, S., Schneider, R.K., McMahon, C., Cowley, G.S., Root, D.E., Ebert, B.L., and Kaelin, W.G., Jr. (2013). (R)-2-hydroxyglutarate is sufficient to promote leukemogenesis and its effects are reversible. Science *339*, 1621–1625.

Lu, C., Venneti, S., Akalin, A., Fang, F., Ward, P.S., Dematteo, R.G., Intlekofer, A.M., Chen, C., Ye, J., Hameed, M., et al. (2013). Induction of sarcomas by mutant IDH2. Genes Dev. *27*, 1986–1998.

Luo, W., Zhong, J., Chang, R., Hu, H., Pandey, A., and Semenza, G.L. (2010). Hsp70 and CHIP selectively mediate ubiquitination and degradation of hypoxia-inducible factor (HIF)-1alpha but Not HIF-2alpha. J. Biol. Chem. *285*, 3651–3663.

Lussey-Lepoutre, C., Hollinshead, K.E., Ludwig, C., Menara, M., Morin, A., Castro-Vega, L.J., Parker, S.J., Janin, M., Martinelli, C., Ottolenghi, C., et al. (2015). Loss of succinate dehydrogenase activity results in dependency on pyruvate carboxylation for cellular anabolism. Nat. Commun. *6*, 8784.

Marie-Egyptienne, D.T., Lohse, I., and Hill, R.P. (2013). Cancer stem cells, the epithelial to mesenchymal transition (EMT) and radioresistance: potential role of hypoxia. Cancer Lett. *341*, 63–72.

Mohammad, F., Weissmann, S., Leblanc, B., Pandey, D.P., Højfeldt, J.W., Comet, I., Zheng, C., Johansen, J.V., Rapin, N., Porse, B.T., et al. (2017). EZH2 is a potential therapeutic target for H3K27M-mutant pediatric gliomas. Nat. Med. *23*, 483–492.

Morin, A., Letouzé, E., Gimenez-Roqueplo, A.P., and Favier, J. (2014). Oncometabolites-driven tumorigenesis: From genetics to targeted therapy. Int. J. Cancer *135*, 2237–2248.

Myszczyszyn, A., Czarnecka, A.M., Matak, D., Szymanski, L., Lian, F., Kornakiewicz, A., Bartnik, E., Kukwa, W., Kieda, C., and Szczylik, C. (2015). The Role of Hypoxia and Cancer Stem Cells in Renal Cell Carcinoma Pathogenesis. Stem Cell Rev. Rep. *11*, 919–943.

Neph, S., Kuehn, M.S., Reynolds, A.P., Haugen, E., Thurman, R.E., Johnson, A.K., Rynes, E., Maurano, M.T., Vierstra, J., Thomas, S., et al. (2012). BEDOPS: high-performance genomic feature operations. Bioinformatics *28*, 1919–1920.

Neri, F., Incarnato, D., Krepelova, A., Rapelli, S., Pagnani, A., Zecchina, R., Parlato, C., and Oliviero, S. (2013). Genome-wide analysis identifies a functional association of Tet1 and Polycomb repressive complex 2 in mouse embryonic stem cells. Genome Biol. *14*, R91.

Nilsson, H., Jögi, A., Beckman, S., Harris, A.L., Poellinger, L., and Påhlman, S. (2005). HIF-2alpha expression in human fetal paraganglia and neuroblastoma: relation to sympathetic differentiation, glucose deficiency, and hypoxia. Exp. Cell Res. *303*, 447–456.

Ohm, J.E., McGarvey, K.M., Yu, X., Cheng, L., Schuebel, K.E., Cope, L., Mohammad, H.P., Chen, W., Daniel, V.C., Yu, W., et al. (2007). A stem cell-like chromatin pattern may predispose tumor suppressor genes to DNA hypermethylation and heritable silencing. Nat. Genet. *39*, 237–242.

Pastor, W.A., Pape, U.J., Huang, Y., Henderson, H.R., Lister, R., Ko, M., McLoughlin, E.M., Brudno, Y., Mahapatra, S., Kapranov, P., et al. (2011). Genome-wide mapping of 5-hydroxymethylcytosine in embryonic stem cells. Nature *473*, 394–397.

Pietras, A., Johnsson, A.S., and Påhlman, S. (2010). The HIF-2α-driven pseudo-hypoxic phenotype in tumor aggressiveness, differentiation, and vascularization. Curr. Top. Microbiol. Immunol. *345*, 1–20.

Putiri, E.L., Tiedemann, R.L., Thompson, J.J., Liu, C., Ho, T., Choi, J.H., and Robertson, K.D. (2014). Distinct and overlapping control of 5-methylcytosine and 5-hydroxymethylcytosine by the TET proteins in human cancer cells. Genome Biol. *15*, R81.

Qin, N., de Cubas, A.A., Garcia-Martin, R., Richter, S., Peitzsch, M., Menschikowski, M., Lenders, J.W., Timmers, H.J., Mannelli, M., Opocher, G., et al. (2014). Opposing effects of HIF1α and HIF2α on chromaffin cell phenotypic features and tumor cell proliferation: Insights from MYC-associated factor X. Int. J. Cancer *135*, 2054–2064.

Quinlan, A.R., and Hall, I.M. (2010). BEDTools: a flexible suite of utilities for comparing genomic features. Bioinformatics *26*, 841–842.

Rampal, R., Alkalin, A., Madzo, J., Vasanthakumar, A., Pronier, E., Patel, J., Li, Y., Ahn, J., Abdel-Wahab, O., Shih, A., et al. (2014). DNA hydroxymethylation profiling reveals that WT1 mutations result in loss of TET2 function in acute myeloid leukemia. Cell Rep. *9*, 1841–1855.

Rose, N.R., McDonough, M.A., King, O.N., Kawamura, A., and Schofield, C.J. (2011). Inhibition of 2-oxoglutarate dependent oxygenases. Chem. Soc. Rev. *40*, 4364–4397.

Roussa, E., and Krieglstein, K. (2004). GDNF promotes neuronal differentiation and dopaminergic development of mouse mesencephalic neurospheres. Neurosci. Lett. *361*, 52–55.

Schlesinger, Y., Straussman, R., Keshet, I., Farkash, S., Hecht, M., Zimmerman, J., Eden, E., Yakhini, Z., Ben-Shushan, E., Reubinoff, B.E., et al. (2007). Polycomb-mediated methylation on Lys27 of histone H3 pre-marks genes for de novo methylation in cancer. Nat. Genet. *39*, 232–236.

Schnepp, A., Komp Lindgren, P., Hülsmann, H., Kröger, S., Paulsson, M., and Hartmann, U. (2005). Mouse testican-2. Expression, glycosylation, and effects on neurite outgrowth. J. Biol. Chem. *280*, 11274–11280.

Selak, M.A., Armour, S.M., MacKenzie, E.D., Boulahbel, H., Watson, D.G., Mansfield, K.D., Pan, Y., Simon, M.C., Thompson, C.B., and Gottlieb, E. (2005). Succinate links TCA cycle dysfunction to oncogenesis by inhibiting HIF-alpha prolyl hydroxylase. Cancer Cell *7*, 77–85.

Sinha, S., Thomas, D., Yu, L., Gentles, A.J., Jung, N., Corces-Zimmerman, M.R., Chan, S.M., Reinisch, A., Feinberg, A.P., Dill, D.L., and Majeti, R. (2015). Mutant WT1 is associated with DNA hypermethylation of PRC2 targets in AML and responds to EZH2 inhibition. Blood *125*, 316–326.

Sousa, B., Pereira, J., and Paredes, J. (2019). The Crosstalk Between Cell Adhesion and Cancer Metabolism. Int. J. Mol. Sci. *20*, 1933.

Stanzel, S., Stubbusch, J., Pataskar, A., Howard, M.J., Deller, T., Ernsberger, U., Tiwari, V.K., Rohrer, H., and Tsarovina, K. (2016). Distinct roles of hand2 in developing and adult autonomic neurons. Dev. Neurobiol. *76*, 1111–1124.

Stark, R., and Brown, G. (2011). DiffBind: Differential binding analysis of ChIP-Seq peak data. In Bioconductor (Cambridge, UK: University of Cambridge).

Svahn, F., Juhlin, C.C., Paulsson, J.O., Fotouhi, O., Zedenius, J., Larsson, C., and Stenman, A. (2018). Telomerase reverse transcriptase promoter hypermethylation is associated with metastatic disease in abdominal paraganglioma. Clin. Endocrinol. (Oxf.) *88*, 343–345.

Thienpont, B., Steinbacher, J., Zhao, H., D'Anna, F., Kuchnio, A., Ploumakis, A., Ghesquière, B., Van Dyck, L., Boeckx, B., Schoonjans, L., et al. (2016). Tumour hypoxia causes DNA hypermethylation by reducing TET activity. Nature *537*, 63–68.

Thomson, J.P., Ottaviano, R., Unterberger, E.B., Lempiäinen, H., Muller, A., Terranova, R., Illingworth, R.S., Webb, S., Kerr, A.R., Lyall, M.J., et al. (2016). Loss of Tet1-Associated 5-Hydroxymethylcytosine Is Concomitant with Aberrant Promoter Hypermethylation in Liver Cancer. Cancer Res. *76*, 3097–3108.

Toyofuku, T., Zhang, H., Kumanogoh, A., Takegahara, N., Suto, F., Kamei, J., Aoki, K., Yabuki, M., Hori, M., Fujisawa, H., and Kikutani, H. (2004). Dual roles of Sema6D in cardiac morphogenesis through region-specific association of its receptor, Plexin-A1, with off-track and vascular endothelial growth factor receptor type 2. Genes Dev. *18*, 435–447.

Turcan, S., Rohle, D., Goenka, A., Walsh, L.A., Fang, F., Yilmaz, E., Campos, C., Fabius, A.W., Lu, C., Ward, P.S., et al. (2012). IDH1 mutation is sufficient to establish the glioma hypermethylator phenotype. Nature *483*, 479–483.

Uchida, T., Rossignol, F., Matthay, M.A., Mounier, R., Couette, S., Clottes, E., and Clerici, C. (2004). Prolonged hypoxia differentially regulates hypoxia-inducible factor (HIF)-1alpha and HIF-2alpha expression in lung epithelial cells: implication of natural antisense HIF-1alpha. J. Biol. Chem. *279*, 14871–14878.

Uribe-Lewis, S., Stark, R., Carroll, T., Dunning, M.J., Bachman, M., Ito, Y., Stojic, L., Halim, S., Vowler, S.L., Lynch, A.G., et al. (2015). 5-hydroxymethylcytosine marks promoters in colon that resist DNA hypermethylation in cancer. Genome Biol. *16*, 69.

Verma, S.K., Tian, X., LaFrance, L.V., Duquenne, C., Suarez, D.P., Newlander, K.A., Romeril, S.P., Burgess, J.L., Grant, S.W., Brackley, J.A., et al. (2012). Identification of Potent, Selective, Cell-Active Inhibitors of the Histone Lysine Methyltransferase EZH2. ACS Med. Chem. Lett. *3*, 1091–1096.

Verma, N., Pan, H., Doré, L.C., Shukla, A., Li, Q.V., Pelham-Webb, B., Teijeiro, V., González, F., Krivtsov, A., Chang, C.J., et al. (2018). TET proteins safeguard bivalent promoters from de novo methylation in human embryonic stem cells. Nat. Genet. *50*, 83–95.

Viré, E., Brenner, C., Deplus, R., Blanchon, L., Fraga, M., Didelot, C., Morey, L., Van Eynde, A., Bernard, D., Vanderwinden, J.M., et al. (2006). The Polycomb group protein EZH2 directly controls DNA methylation. Nature *439*, 871–874.

Wang, Y., Xiao, M., Chen, X., Chen, L., Xu, Y., Lv, L., Wang, P., Yang, H., Ma, S., Lin, H., et al. (2015). WT1 recruits TET2 to regulate its target gene expression and suppress leukemia cell proliferation. Mol. Cell *57*, 662–673.

Wassef, M., Luscan, A., Aflaki, S., Zielinski, D., Jansen, P.W.T.C., Baymaz, H.I., Battistella, A., Kersouani, C., Servant, N., Wallace, M.R., et al. (2019). EZH1/2 function mostly within canonical PRC2 and exhibit proliferation-dependent redundancy that shapes mutational signatures in cancer. Proc. Natl. Acad. Sci. USA *116*, 6075–6080.

Williams, K., Christensen, J., Pedersen, M.T., Johansen, J.V., Cloos, P.A., Rappsilber, J., and Helin, K. (2011a). TET1 and hydroxymethylcytosine in transcription and DNA methylation fidelity. Nature *473*, 343–348.

Williams, S.C., Karajannis, M.A., Chiriboga, L., Golfinos, J.G., von Deimling, A., and Zagzag, D. (2011b). R132H-mutation of isocitrate dehydrogenase-1 is not sufficient for HIF-1α upregulation in adult glioma. Acta Neuropathol. *121*, 279–281.

Wu, H., D'Alessio, A.C., Ito, S., Wang, Z., Cui, K., Zhao, K., Sun, Y.E., and Zhang, Y. (2011). Genome-wide analysis of 5-hydroxymethylcytosine distribution reveals its dual function in transcriptional regulation in mouse embryonic stem cells. Genes Dev. *25*, 679–684.

Xiao, M., Yang, H., Xu, W., Ma, S., Lin, H., Zhu, H., Liu, L., Liu, Y., Yang, C., Xu, Y., et al. (2012). Inhibition of α-KG-dependent histone and DNA demethylases by fumarate and succinate that are accumulated in mutations of FH and SDH tumor suppressors. Genes Dev. *26*, 1326–1338.

Xu, B., Zeng, D.Q., Wu, Y., Zheng, R., Gu, L., Lin, X., Hua, X., and Jin, G.H. (2011). Tumor suppressor menin represses paired box gene 2 expression via Wilms tumor suppressor protein-polycomb group complex. J. Biol. Chem. *286*, 13937–13944.

Yamamoto, A., Uchiyama, K., Nara, T., Nishimura, N., Hayasaka, M., Hanaoka, K., and Yamamoto, T. (2014). Structural abnormalities of corpus callosum and cortical axonal tracts accompanied by decreased anxiety-like behavior and lowered sociability in spock3- mutant mice. Dev. Neurosci. *36*, 381–395.

Zhang, Y., Liu, T., Meyer, C.A., Eeckhoute, J., Johnson, D.S., Bernstein, B.E., Nusbaum, C., Myers, R.M., Brown, M., Li, W., and Liu, X.S. (2008). Model-based analysis of ChIP-Seq (MACS). Genome Biol. *9*, R137.

Zhao, S., Lin, Y., Xu, W., Jiang, W., Zha, Z., Wang, P., Yu, W., Li, Z., Gong, L., Peng, Y., et al. (2009). Glioma-derived mutations in IDH1 dominantly inhibit IDH1 catalytic activity and induce HIF-1alpha. Science *324*, 261–265.

STAR★METHODS

KEY RESOURCES TABLE

REAGENT or RESOURCE	SOURCE	IDENTIFIER
Antibodies		
anti-H3K27me3	Diagenode	Cat# C15410069, RRID: AB_2814977
anti-5mC	Calbiochem	Cat# NA81-50UG, RRID: AB_213180
anti-5hmC	Active Motif	Cat# 39769, RRID: AB_10013602
anti-ssDNA	Millipore	Cat# MAB3299, RRID: AB_94795
biotinylated secondary antibody	VECTOR	Cat# BA-1000, RRID: AB_2313606
HRP-conjugated mouse secondary antibodies	Biovision	Cat# 6402-05, RRID: AB_657968
HRP-conjugated rabbit secondary antibodies	Biorad	Cat# 170-6515, RRID: AB_11125142
anti-actin	Sigma-Aldrich	Cat# A5316, RRID: AB_476743
anti-TET1	Millipore	Cat# 09-872, RRID: AB_10806199
anti-TET2	Proteintech	Cat# 21207-1-AP, RRID: AB_10734584
anti-TET3	Active motif	Cat#61744 clone 23B9; RRID: AB_2793753
anti-HIF2α	Abcam	Cat# ab8365, RRID: AB_306519
anti-HIF2α	Abcam	Cat# ab109616, RRID: AB_11156727
Anti-H3K27me3	Active Motif	Cat# 39156, RRID: AB_2636821
anti-H3-Cterminal	Active Motif	Cat# 39451, RRID: AB_2793242
Anti-Hif2α antibody	R&D Systems	Cat# AF2997, RRID: AB_2098218
Donkey anti-rabbit secondary antibody, Alexa Fluor 594	Invitrogen	Cat# A-21207, RRID: AB_141637
Bacterial and Virus Strains		
pLKO.1 empty vector	Sigma-Aldrich	
Tet1 shRNA pLKO.1-puro vector	Sigma-Aldrich	TRCN0000341849
Tet2 shRNA pLKO.1-puro vector	Sigma-Aldrich	TRCN0000250894
HIF1α pLKO.1-puro vector	Sigma-Aldrich	TRCN0000232220
HIF2α pLKO.1-puro vector	Sigma-Aldrich	TRCN000082304
shSCR pLKO.1-puro vector	Sigma-Aldrich	SHC016
Biological Samples		
HUMAN: Frozen paraganglioma samples	COMETE Collection	N/A
Chemicals, Peptides, and Recombinant Proteins		
DMEM (Dulbecco Modified Eagle Medium)	GIBCO	31966-021
Fetal bovine serum	GIBCO	10270
Penicillin/Streptomycin	GIBCO	15140-122
UNC1999	Sigma-Aldrich	SML0778
UNC2400	SGC	https://www.thesgc.org/chemical-probes
GSK343	Sigma-Aldrich	SML0766
DMSO	Sigma-Aldrich	D4540
trypsin-EDTA 0.05%	GIBCO	25300-054
puromycin	Invivogen	CAS 58-58-2
polybrene	Sigma-Aldrich	TR-1003-G
proteinase K	Sigma-Aldrich	1245680500
PBS	GIBCO	10010-015
QiaAmp DNA mini kit,	QIAGEN	51306
DNA coating buffer	Thermofisher	17250
Kathon	Supelco	5-00127

(*Continued on next page*)

Continued

REAGENT or RESOURCE	SOURCE	IDENTIFIER
Tween 20	Sigma-Aldrich	P1379
Streptavidin HRP	BD Bioscience	554066
RIPA buffer	Abcam	Ab156034
NuPAGE® Novex 4–16% Bis-Tris gradient gel	Invitrogen	NP0335BOX
PVDF membrane	Millipore	IPVH00010
nitrocellulose membrane	Amersham	10600001
H2SO4	VWR	20700.298
trichloroacetic acid	Sigma-Aldrich	T6399
acetone	VWR	E646-1L
formaldehyde	VWR	11699404
triton buffer	Sigma-Aldrich	T8787
Phalloidin-TRITC toxin	Sigma-Aldrich	#P1951
vectashield with Dapi	VECTOR	H-1200
Critical Commercial Assays		
AllPrep extraction kit	QIAGEN	80204
NEXTflex PCR-Free DNA Sequencing kit	Diagenode	ref. C02010021
MagMeDIP kit	Diagenode	C02010021
Genomic DNA Clean & Concentrator kit	Zymo Research	ref. D4010
RNeasy plus mini-kit	QIAGEN	74134
iScript enzyme	BioRad	1708891
TrueMethyl 24 kit	Cambridge Epigenetix	N/A
SuperScript SybrGreen	BioRad	#1725151
iDeal ChIP-qPCR kit	Diagenode	#C01010180
GenElute Mammalian genomic DNA kit	Sigma-Aldrich	#G1N350
Genomic DNA Clean & Concentrator kit	Zymo Research	ref. D4010
Deposited Data		
MeDIP-seq, RRBS and oxRRBS data	European Genome Phenome Archive	EGA: EGAS00001004252
Experimental Models: Cell Lines		
MOUSE: imCC WT	Letouzé et al., 2013	N/A
MOUSE: imCC Sdhb−/−	Letouzé et al., 2013	N/A
Experimental Models: Organisms/Strains		
NMRI nude mice	Janvier Lab	N/A
Oligonucleotides		
Oligonucleotides	This study	Table S3
Software and Algorithms		
bowtie2	Langmead and Salzberg, 2012	http://bowtie-bio.sourceforge.net/bowtie2/index.shtml
Picard Tools	Broadinstitute	http://picard.sourceforge.net
SAMtools	Li et al., 2009	http://samtools.sourceforge.net
MACS	Zhang et al., 2008	https://github.com/taoliu/MACS
bedtools	Quinlan and Hall, 2010	https://bedtools.readthedocs.io/en/latest/
GAT	Heger et al., 2013	https://gat.readthedocs.io/en/latest/
Bioconductor DiffBind package	Stark and Brown, 2011	https://bioconductor.org/packages/release/bioc/html/DiffBind.html
Bedmap tool from the BEDOPS suite	Neph et al., 2012	https://bedops.readthedocs.io/en/latest/
Bioconductor DESeq package	Anders and Huber, 2010	https://bioconductor.org/packages/release/bioc/html/DESeq.html

(*Continued on next page*)

Continued

REAGENT or RESOURCE	SOURCE	IDENTIFIER
FastQC	Babraham Bioinformatics	http://www.bioinformatics.babraham.ac.uk/projects/fastqc/
tophat2	Kim et al., 2013	https://ccb.jhu.edu/software/tophat/index.shtml
HTSeq	Anders et al., 2015	https://htseq.readthedocs.io/en/release_0.11.1/
R statistical software	The R Foundation	https://cran.r-project.org
BS-Seeker2	Guo et al., 2013	https://github.com/BSSeeker/BSseeker2
methylKit package	Akalin et al., 2012	https://bioconductor.org/packages/release/bioc/html/methylKit.html
R code from the GSEA website		https://www.gsea-msigdb.org/gsea/index.jsp
PRISM 8	Graphpad	https://www.graphpad.com/scientific-software/prism/
NIS-advanced imaging software	Nikon	https://www.microscope.healthcare.nikon.com/products/software/nis-elements
Other		
MSigDB database version 5.1	UCSD, Broad Institute	https://www.gsea-msigdb.org/gsea/msigdb/index.jsp

LEAD CONTACT AND MATERIALS AVAILABILITY

Further information and requests should be directed to and will be fulfilled by the Lead Contact, Judith Favier (judith.favier@inserm.fr). This study did not generated new unique reagents.

EXPERIMENTAL MODEL AND SUBJECT DETAILS

Patients and tumor samples

We used tumor samples from 4 patients (see gender and age of the patients in the table Data generated) recruited in the COMETE network and previously characterized by HM27 methylome Chip and transcriptomic arrays in Letouze et al., 2013. This seminal paper identified 3 clusters: M1 (mainly SDH tumors), M2 (contains most VHL tumors), and M3 (included NF1, RET, and sporadic tumors). To be homogeneous, 2 *NF1*-mutated pheochromocytomas were selected in cluster M3, and compared to 2 *SDHB*-mutated pheochromocytomas from cluster M1.

Mammalian cell line

imCC were cultured in DMEM (Dulbecco Modified Eagle Medium, GIBCO) with 10% FBS (Fetal bovine serum, GIBCO) and 1% antibiotics (penicillin/streptomycin, GIBCO). Cells were grown at 37°C, in 5% CO2.

Data generated

Genotype	Sample	Gender	Age at surgery	meDIP-seq	oxRRBS	RRBS	Transcriptomic
SDHB-WT (*NF1*-mut)	Human tumor HS_033	Female	66	yes	yes	yes	arrays
SDHB-WT (*NF1*-mut)	Human tumor HS_045	Female	52	yes	yes	yes	arrays
SDHB-mut	Human tumor HS_144	Male	28	yes	yes	yes	arrays
SDHB-mut	Human tumor HS_196	Female	31	yes	yes	yes	arrays
$Sdhb^{lox/lox}$ (WT)	imCC	Female		yes	yes	yes	RNA-seq
$Sdhb^{-/-}$	imCC	Female		yes	yes	yes	RNA-seq
$Tet1{+}Tet2^{KD}$	imCC Cl74	Female		no	no	yes	no

Mouse model

Athymic nude NMRI female mice (6-weeks old, Janvier Labs, France) were maintained in specific pathogen-free conditions in a temperature-controlled environment with 12 h light, 12 h dark cycles and received food and water *ad libitum* at the animal facility of the PARCC Paris, France. Animal experiments were performed by certified personal following the French law on animal experimentation n°2013-118 and were approved by the French Ethical Committee (#16922-2017122215408962v4).

METHOD DETAILS

MeDIP-seq analysis

gDNA extracted with AllPrep extraction kit (QIAGEN) was fragmented by sonication and used to prepare non-amplified DNA libraries with the NEXTflex PCR-Free DNA Sequencing kit. 1ug of the equimolar pool of all sample libraries (with internal IP "spike-in" controls added) was kept as input, and 3ug was used for meDIP-seq with MagMeDIP kit (Diagenode ref. C02010021). Immunoprecipitation was conducted following manufacturer instructions. Briefly, after heat-denaturation, DNA was incubated overnight with magnetic beads coated with anti-5mC antibody. Beads were washed and then eluted by proteinase K digestion of the antibody. Eluted DNA was further purified with Genomic DNA Clean & Concentrator kit (Zymo Research ref. D4010). IP efficiency and specificity was verified by qPCR targeting the internal controls. Sequencing was performed on an Illumina HiSeq2000 as paired-end 75 bp reads.

Fastq files were aligned to the reference human genome hg19 and mouse genome mm10 with bowtie2 (Langmead and Salzberg, 2012). We filtered and kept only reads mapping to one location. Duplicated reads were removed from the datasets using Picard Tools (http://picard.sourceforge.net) and total number of reads were down-sized to the minimum available read count for each type of samples (MeDIP 48.10^6 reads and INPUT 74.10^6 reads for human samples, and MeDIP 62.10^6 reads and INPUT 73.10^6 reads for mouse samples) using SAMtools (Li et al., 2009). Peaks were identified using MACS (Zhang et al., 2008) (-s 50 -p 10^{-5} -m 10,30) and associated to closest TSS using bedtools (Quinlan and Hall, 2010). We used GAT (Heger et al., 2013) to perform genomic association analysis of our peaks with gene annotations and CpG island, shore, and shelf annotation. We used the Bioconductor *DiffBind* package (Stark and Brown, 2011) to define a common set of peaks between all samples (peaks common to at least two samples are considered). We used the bedmap tool from the BEDOPS suite (Neph et al., 2012) to collect read counts for all MeDIP and INPUT samples within the common set of peaks. We created a normalized binding matrix with, for each peak and MeDIP sample, a read count normalized with peak size. The log2 normalized binding matrix from the 1,000 most variant peaks (based on standard deviation of the normalized read counts) was used to classify the samples according to their binding patterns using hierarchical clustering (with Euclidian distance and Ward method). We used the Bioconductor *DESeq* package (Anders and Huber, 2010) to test for differential read counts between samples, without correcting for size factors as libraries had been previously down-sized.

RNA-seq analysis

Quality of reads was assessed for each sample using FastQC (http://www.bioinformatics.babraham.ac.uk/projects/fastqc/). Fastq files were aligned to the reference Human genome hg19/GRCh37 or to the reference Mouse genome mm10 with tophat2 (-p 16 -r 150 -g 2–library-type fr-firststrand) (Kim et al., 2013). We removed reads mapping to multiple locations. We used HTSeq (Anders et al., 2015) to obtain the number of reads associated to each gene in the Gencode vM9 (Mouse) database, restricting to protein-coding genes, antisense and lncRNAs. We used the Bioconductor DESeq package (Anders and Huber, 2010) to import raw HTSeq counts for each sample into R statistical software and extract the count matrix. After normalizing for library size, we normalized the count matrix by the coding length of genes to compute FPKM scores (number of fragments per kilobase of exon model and millions of mapped reads). We used the Bioconductor *DESeq* package to obtain size factors and dispersion estimates, and perform differential expression analysis.

oxRRBS and RRBS Analyses

RRBS was performed by Integragen SA (Evry, France), as previously described (Letouze et al.). This analysis does not distinguish 5mC from 5hmC, and considering the low levels of 5hmC compared to 5mC, it represents a good estimation of 5mC levels.

oxRRBS analysis is required for 5hmC quantification. An additional oxidative step converts 5hmC to 5fC which is sensitive to bisulfite treatment, unlike 5mC and 5hmC. Each sample is thus run for both RRBS and oxRRBS procedures in parallel. 5hmC levels are calculated by subtracting RRBS – oxRRBS signals.

oxRRBS was performed by Integragen SA (Evry, France), as described in Letouzé et al. (2013) for the MspI Reduced Representation part, and following the TrueMethyl 24 kit manufacturer protocol user guide version 3.1 (https://www.nugen.com/support/user-manuals) for the OxBS part. In brief, 4 μg of genomic DNA plus CeGX Sequencing Control (3% W/W) were digested with MspI (NEB) then SPRI 2.2X purified. After end-repair, A-tailing, and ligation to methylated Illumina adapters, the library fragments of 40–220 bp were gel isolated, and oxidative bisulfite- and only bisulfite-converted DNA templates were generated using the TrueMethyl 24 kit (Cambridge Epigenetix) for each sample according to the manufacturer's instructions. Last, oxRRBS- and RRBS-converted DNA were PCR amplified with 16 cycles, SPRI 1.8X purified and sequenced on an Illumina HiSeq2000 or HiSeq4000 as paired-end 75 bp reads.

We generated approximately 30 millions uniquely aligned reads for each sample, which covered ≈8 million CpG (Figure S1C; Table S2). We used BS-Seeker2 (Guo et al., 2013) to map RRBS data to the human genome hg19/GRCh37 or Mouse genome mm10 and retrieve the number of methylated and unmethylated cytosines at each covered CpG site. Methylation rates were then integrated across CpG island (CGI)-based and gene-based features. CGI-based features were defined as follows: CpG islands (from UCSC database hg19/GRCh37 or Mouse mm10), shores (2 kb on each side of the island) and shelves (2 kb on each side of the shores). DNA methylation outside CpG islands was analyzed by grouping CpG sites not located in CGI-based features every 100kb window. Gene-based features were defined based on Ensembl *Homo sapiens* GRCh37.p13 or *Mus musculus* GRCm38.78

assembly. We calculated for each gene the methylation rate across the promoter region (TSS ± 500bp) and the gene body (Figure S1A).

5hmC detection using (ox)RRBS data

To detect the presence of 5hmC, we compared the proportions of converted C bases between the RRBS and oxRRBS experiments in each CGI- and gene-based feature using Fisher's exact tests, corrected for multiple testing using Benjamini Hochberg procedure. We verified that >90% of features with a significant difference ($q < 0.05$) had an excess of converted bases in the oxRRBS experiment, as expected, indicating that we detected true 5hmC signal and not random noise. Finally, we considered that 5hmC was detected in a feature when the q value of the Fisher's exact test was < 0.05, with ≥ 100 CpGs analyzed, and we estimated the 5hmC rate as the delta between the proportions of converted C bases in the RRBS and oxRRBS experiments. For other features the 5hmC rate was considered to be zero.

Differential (hydroxy)methylation analysis

We compared methylation rates across all CGI-based and gene-based features (covered by at least 50 reads). q values were computed by comparing the number of (hydroxy) methylated and un(hydroxy)methylated reads in each condition using a logistic regression and the SLIM method for pvalue adjustment, as implemented in the methylKit package (Akalin et al., 2012). We also calculated the methylation rate difference (delta) between each pair of test and reference sample. We considered as differentially methylated every region with a q-value < 0.05 and a methylation delta >0.05 or <−0.05 in at least 80% of test-reference pairs.

Gene set enrichment analysis

We used the GSEA method (Subramanian et al., 2005) to identify gene sets overrepresented among up/down- regulated and hyper/hypomethylated genes. The GSEA method calculates an enrichment score that reflects the degree to which genes belonging to a given gene set are overrepresented at the top or bottom of a gene list, ranked for example by their expression fold-change between two conditions. The statistical significance (nominal p value) of the enrichment score is derived using a permutation test procedure, and p values across gene sets are adjusted for multiple testing. We used the R code downloaded from the GSEA website (https://www.gsea-msigdb.org/gsea/index.jsp) to calculate enrichment scores, significance p values and q-values, which we adapted to be able to provide any ranked gene list as input. For RNA-seq analyses, genes were ranked according to their expression fold-change between the two conditions (e.g., *Sdhb*−/− versus wild-type cells). For MeDIP-seq analyses, genes were ranked according to the fold-change of methylation signal within their TSS region (TSS ± 500 bp) between the two conditions. For RR(ox)BS analyses, genes were ranked according to the methylation rate difference (delta) within their TSS region (TSS ± 500 bp) between the two conditions. We downloaded gene sets from the MSigDB database (version 5.1) and restricted our analysis to the hallmark (H), curated (C2) and oncogenic (C6) gene sets.

Inhibition of PRC2 activity

When stated they WT or *Sdhb*−/− imCC were treated with GSK343 or vehicle (DMSO) for 5 to 7 passages (17 to 24 days), or treated with UNC1999, UNC2400 or vehicule (DMSO) for 15 days, or cultured for indicated times at 2% O2 in a nitrogen-supplemented hypoxic incubator. For GSK343 treatments, the classical of dose of 3 μM was chosen (Mohammad et al., 2017) as it allows a potent EZH2 inhibition (IC_{50} = 4nM) and has been described as the growth IC_{50} value (2.9 μM) in the most sensitive cell lines studied (prostate cancer cell line LNCaP) (Verma et al., 2012). For UNC1999 and UN2400 (Konze et al., 2013) we chose a dose of 1 μM as used in Wassef et al. (2019).

Proliferation assay

Proliferation curves were established on a 7 days period. When stated, cells were preincubated for 72h in normoxia or hypoxia before cell counting. Proliferation index were calculated as the differential coefficient of the linear regression from cell proliferation curves.

Adhesion assay

After complete detachment from their plate using trypsin-EDTA 0.05% (GIBCO), cells were plated in 12-wells dishes. Cell adhesion was analyzed by taking picture 1 to 3 h post-seeding. Percentage of adhesive cells at 1 to 1.5 h allowed accurate comparison of WT to *Sdhb*−/− cells. 3 h were more appropriate to distinguish Tet1+Tet2^{KD} cells from shSCR cells, but at that time point, 100% *Sdhb*−/− cells were adherent, in normoxia as in hypoxia.

Wound scratch assay

Wound scratch assays were performed as described elsewhere (Loriot et al., 2015) and analyzed using ImageJ software or using Nikon videomicroscope and NIS-advanced imaging software. The experiments were performed in triplicates.

shRNA stable transduction

Lentiviral constructs were purchased at Sigma-Aldrich. pLKO.1 is the parental viral vector without shRNA. WT imCC (30000) were infected in a serum-free medium containing 8 μg/mL polybrene by either 10 MOI of Tet1 (TRCN0000341849) and 10 MOI of Tet2

(TRCN0000250894) shRNA vectors, or 20 MOI of scramble shRNA vector targeting no known mammalian genes (shSCR SHC016). 48 h post-infection, transduced cells were selected by puromycin treatment (4 μg/mL) for 13 days and sub-cloned. Clones were screened for Tet1 and Tet2 knockdown by qRT-PCR and protein inhibition in selected clones was confirmed by Western Blot.

Sdhb−/− imCC (50,000) were seeded in 48-well plates. 24 h later, cells were washed twice with PBS and transduced with 10 MOI of lentiviral vectors (pLKO.1-puro, Sigma-Aldrich) encoding shRNAs for HIF1α (TRCN0000232220) or HIF2α (TRCN000082304) in the presence of polybrene [8 μg/ml] and serum-free medium. Double transductions (HIF1α +HIF2α) were performed at a MOI of 20. 24 h later, fresh complete medium was added and selection was started with puromycin [4 μg/ml] for wild-type or [2 μg/ml] for *Sdhb*−/−. After 1 week of selection, cells were trypsinized and amplified. Then, to obtain clones, a limiting dilution assay was performed for each condition in 96-well plates. Clones were screened for HIF2 or HIF1+HIF2 knockdown by qRT-PCR and HIF2α protein inhibition in selected clones was confirmed by Western Blot.

Reversed Transcription and Quantitative Real-Time PCR

Total RNAs were extracted from cell pellets using RNeasy plus mini-kit (QIAGEN) as described by the manufacturer. Reverse transcription was performed using random primers and iScript enzyme (BioRad), during 30 mn at 42°C. qRT-PCR was run with SuperScript SybrGreen (BioRad) and normalization was performed with Ubc, B2m and 18S amplifications, and comparisons were calculated using the ΔΔCt method. Primers' sequences were as follows:

Ubc: F 5′-AGCCCAGTGTTACCACCAAG-3′; R 5′-ACCCAAGAACAAGCACAAG-3′;
18 S: F 5′-CGCGGTTCTATTTTGTTGGT-3′; R 5′-AACCATAAACGATGCCGAC-3′;
B2m: F 5′-ATTCACCCCCACTGAGACTG-3′; R 5′-TGCTATTTCTTTCTGCGTGC-3′
Hand2: F 5′-CCAGCTACATCGCCTACCTC-3′; R 5′-TGGTTTTCTTGTCGTTGCTG-3′
Gdnf: F 5′-CTGTCTGCCTGGTGTTGCT-3′; R 5′-CTGCCGCTTGTTTATCTGGT-3′
Wnt11: F 5′-TCCGATGCTCCTATGAAGGT-3′; R 5′-CTGACAGGTAGCGGGTCTTG-3′
Sema6d: F 5′-GCTTCCCAGAAGACGATGAG-3′; R 5′-CTGTTTGGGGGATTTCATTT-3′
Stmn2: F 5′-CTACGACGACATGGAGGTGA-3′; R 5′-CCTCTTCTCTGCCAACTGCT-3′
Spock2: F 5′-CCATCGGTTGGATGTTCTCT-3′; R 5′-GACACCTGGCTTCTTCTTGG-3′
Spock3: F 5′-AGGATTCACTTGGCTGGATG-3′; R 5′-TTTATCCCCTGTCGCTTCTG-3′
Snai1: F 5′-TGGAAAGGCCTTCTCTAGGC-3′; R 5′-AAAAGCACGGTTGCAGTGG-3′
Twist1: F 5′-GACTCCAAGATGGCAAGCTG-3′; R 5′-TTCTCTGGAAACAATGACATCTAGGT-3′
Cdh2: F 5′-GAAGATGTTTACAGCGCAGTCTT-3′; R 5′-CTCGCTGCTTTCATACTGAACTT-3′
Epas1: F 5′-AGGGCCACAGCAAAGAGAG-3′; R 5′-CATCACGGGATTTCTCCTTC-3′
Glut1: F 5′-AAACATGGAACCACCGCTAC-3′; R 5′-GGAGAAGCCCATAAGCACAG-3′
Hif1a: F 5′-TCAGCATACAGTGGCACTCA-3′; R 5′-AAGGGAGCCATCATGTTCCA-3′

ChIP-qPCR

Chromatin immunoprecipitation was performed on $1*10^6$ cells using the iDeal ChIP-qPCR kit (Diagenode #C01010180) following manufacturer instructions with 1 μL of anti-H3K27me3 antibody (Diagenode #C15410069) or 1 μL of rabbit IgG from the kit as a negative control. qPCR was performed using the following primer pairs: Hand2 F8/Hand2 R8; Hand2 F3/Hand2 R3; Binding site for PRC1 on Gdnf (https://www.chipprimers.com): Gdnf F1/Gdnf R1; Binding site for PRC2 on Gdnf (https://www.chipprimers.com):Gdnf F2/Gdnf R2; Wnt11 F/Wnt11 R; Sema6d-Iso1 F/Sema6d-Iso1 R; Sema6d-Iso2 F/Sema6d-Iso2 R; Stmn2 F/Stmn2 R; Spock2 F/Spock2 R; Spock3 F/Spock3 R. Primers sequences are detailed in Table S3.

Results of immunoprecipitation were represented as percentage of input. Experiments were repeated 3 times.

5mC and 5hmC ELISA

Colorimetric detection of global levels of 5mC and 5hmC was performed by ELISA. Briefly, 1 μg of purified (QiaAmp DNA mini kit, QIAGEN) DNA was added to 1mL of DNA coating buffer (Thermofisher). After denaturation, 200 μL of DNA (ELISA 5hmC and ssDNA) or 100 μL of DNA + 100 μL of coating buffer (ELISA 5mC) were dropped in duplicates in a 96-well plate and incubated for 2 h at 37°C. After blocking for 30 min with PBS 0.5% BSA 0.05% Kathon, anti-5mC (Calbiochem NA81 1/5000), anti-5hmC (Active Motif #39769 1/200) or anti-ssDNA (Millipore MAB3299 1/200), and secondary antibodies were added to the wells and incubated overnight at 4°C. Antibodies were diluted in blocking buffer supplemented with 0.1% Tween 20. Finally, Avidin HRP (BD Bioscience) 1/2500 was incubated for 30 mn and reaction was developed using TMB and stopped with 1N H2SO4. The absorbance was read at 450 nm. 5mC and 5hmC levels were normalized by absorbance of ssDNA ELISA. Experiments were repeated 3 times.

Western Blot analysis

Total proteins were extracted in RIPA buffer, resolved on NuPAGE® Novex 4%–16% Bis-Tris gradient gel (Invitrogen), transferred on PVDF membrane (for TET western blotting) or nitrocellulose membrane (for HIF western blotting). After blocking in PBS-milk solution (5%), membranes were incubated with specific primary antibodies, followed by incubation with corresponding HRP-conjugated secondary antibodies. The antibodies used were: anti-actin (Sigma-Aldrich A5316 1/50000), anti-TET1 (Millipore #09-972 1/500),

anti-TET2 (Proteintech #21207-1-AP 1/400), anti-TET3 (Active motif #61744 clone 23B9 1/400), anti-HIF2α (Abcam #ab8365 1/1000; Figure 6) or, anti-HIF2α (Abcam ab109616, 1/500; Figure 7).

For H3K27me3 and H3-Cterminal western blots, proteins were extracted by acidic lysis with 0,2M H2SO4, and precipitated with trichloroacetic acid. Pellets were washed with acetone and resuspended in diluted loading buffer and sonicated. Western blot conditions were identical. Proteins were transferred on nitrocellulose membrane. Anti-H3K27me3 (Active Motif #39156) was diluted 1/1000 and anti-H3-Cterminal (Active Motif #39164) was diluted 1/2000.

Fluorescent staining

Actin staining was performed on cultured cells fixed for 5 mn with ice cold 4% formaldehyde and permeabilized with 0.5% triton buffer for 10 mn. Phalloidin-TRITC toxin (Sigma #P1951) diluted 1/1000 was incubated for 1h and washed before mounting the coverslip in vectashield with Dapi. Fluorescence was observed on a confocal microscope and 13 z stacks of 0.5 μm were merged.

Hif2α immunofluorescence was performed on cultured cells fixed for 5 mn with ice cold 4% formaldehyde. After blocking for 30 mn with PBS 1% BSA 0.1% triton, coverslips were incubated of 2h with Hif2α antibody (R&D Systems #AF2997) diluted 1/100 in blocking buffer. Primary antibody was washed and coverslips were blocked in PBS 1% BSA and incubated for 2h with secondary antibody before mounting in vectashield with Dapi.

In vivo metastasis assay

Tet1+Tet2 KD imCC were cultured for 72h at 21% O_2 (normoxia) or 2% O_2 (hypoxia), and subsequently trypsinized, centrifuged, and resuspended in PBS before injection. 10^6 cells were injected in the tail vein of immunocompromised NMRI nude mice. Two different clones of *Tet1+Tet2 KD* imCC were injected in 10 mice per clone, 5 mice for normoxic cells and 5 for hypoxic cells. 41 days after inoculation, mice were sacrificed and lungs were snap-frozen in liquid nitrogen. Genomic DNA extraction was performed on entire lungs using GenElute Mammalian genomic DNA kit (Sigma #G1N350). Metastatic burden was quantified by qPCR using primer pairs specific for the loxP site present in imCC (Letouzé et al., 2013) (but absent from mice lungs):

Forward primer in Sdhb intron 1 and Reverse primer in Sdhb intron1 and loxP site (Table S3).

We previously verified in gDNA extracted from normal mouse tissue that this primer pair does not allow any DNA amplification (data not shown). 18S primer pair was used for normalization.

QUANTIFICATION AND STATISTICAL ANALYSIS

Data are represented as mean (of at least 3 independent experiments) ± SEM (standard error of the mean). Student tests were performed using PRISM software. For additional information, see Table S4.

DATA AND CODE AVAILABILITY

All raw sequence data have been deposited to the European Genome Phenome Archive. The accession number for the MeDIP-seq, RRBS, and oxRRBS data reported in this paper is EGA: EGAS00001004252.

Cell Reports, Volume *30*

Supplemental Information

TET-Mediated Hypermethylation Primes SDH-Deficient Cells for HIF2α-Driven Mesenchymal Transition

Aurélie Morin, Judith Goncalves, Sophie Moog, Luis-Jaime Castro-Vega, Sylvie Job, Alexandre Buffet, Marie-Joséphine Fontenille, Justine Woszczyk, Anne-Paule Gimenez-Roqueplo, Eric Letouzé, and Judith Favier

TET-mediated hypermethylation primes SDH-deficient cells for HIF2α-driven mesenchymal transition

Aurélie Morin, Judith Goncalves, Sophie Moog, Luis-Jaime Castro-Vega, Sylvie Job, Alexandre Buffet, Marie-Joséphine Fontenille, Justine Woszcyk, Anne-Paule Gimenez-Roqueplo, Eric Letouzé and Judith Favier

Supplementary data

- **Figure S1**
- **Figure S2**
- **Figure S3**
- **Figure S4**
- **Figure S5**
- **Figure S6**
- **Figure S7**
- **Supplemental Table S2**
- **Supplemental Table S3 – Oligonucleotides**
- **Supplemental Table S4 – Statistical section**

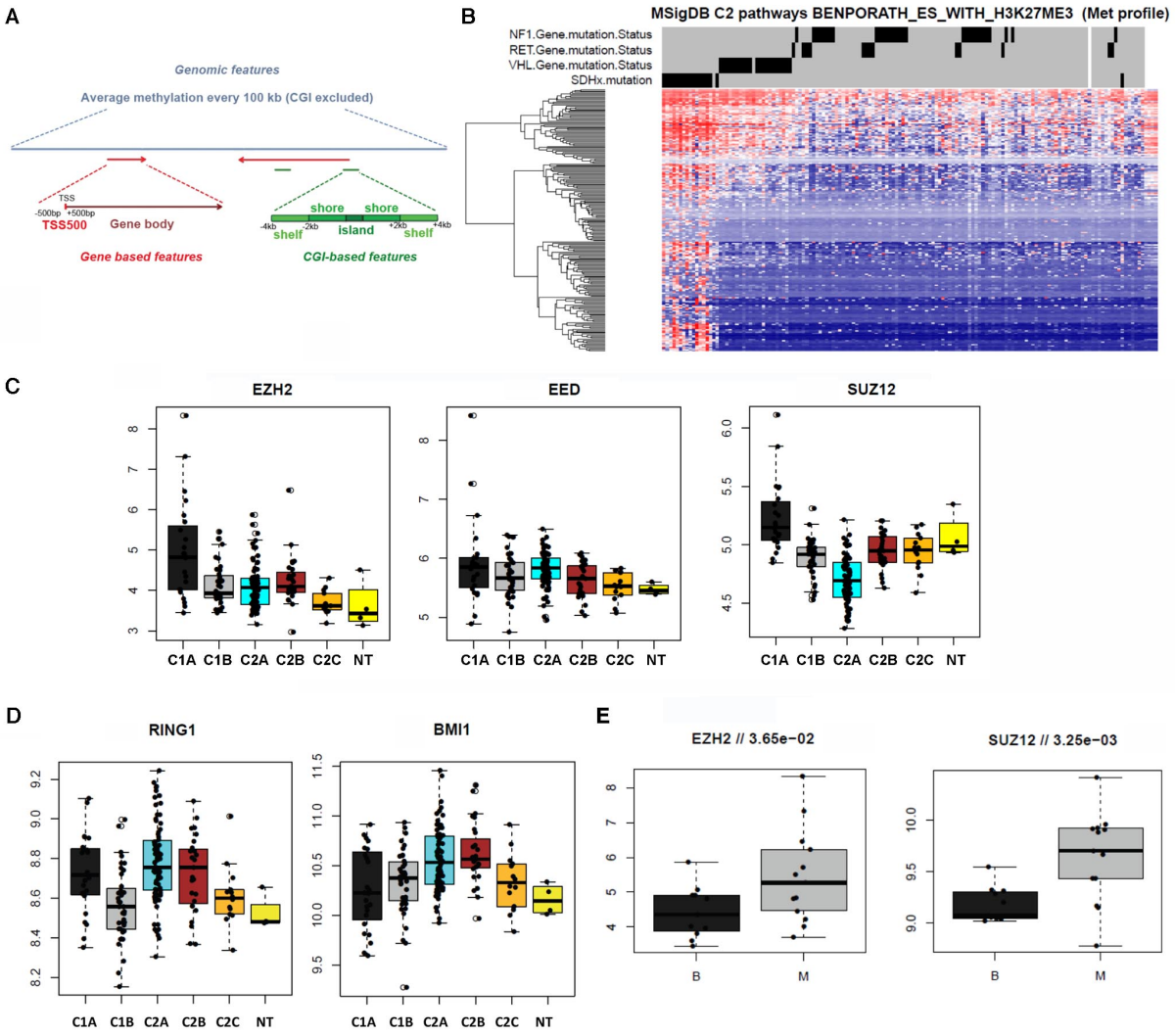


Figure S1. Related to Figure 1. Polycomb pathway in SDH-deficient tumors. A, Description of genomic features used to analyze meDIP-seq and (ox)RRBS data. **B,** Heatmap of DNA methylation obtained from the methylome array data fromLetouzé et al., 2013, restricted to the gene set "BENPORATH_ES_WITH_H3K27ME3". **C,** Microarray-based expression analysis of PRC2 components EZH2, EED and SUZ12 in a cohort of 4 non-tumoral samples and 145 PPGL tumors. Expression clusters have been described in Burnichon et al., 2011. EZH2 and SUZ12 are overexpressed in C1A cluster encompassing tumors with SDH deficiency. **D,** Expression of PRC1 components RING1 and BMI1 in the same cohort. No overexpression of RING1 or BMI1 is observed in C1A cluster. **E,** Microarray-based expression analysis of PRC2 components EZH2 and SUZ12 in the same cohort, comprising 130 benign (B) and 15 metastatic (M) tumors.

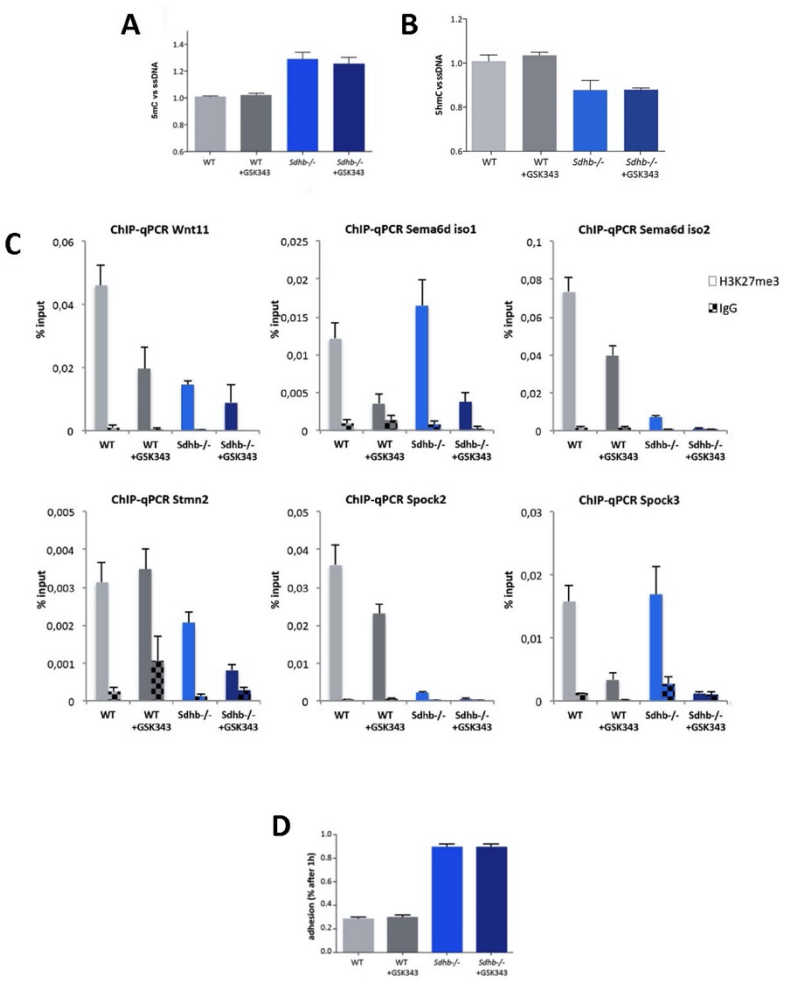


Figure S2. Related to Figure 2. Effects of PRC2 inhibition in imCC. A, B, Quantification of global 5mC and 5hmC levels by ELISA in cells treated with 3µM GSK343 or vehicle for 5 to 7 passages (mean of 3 experiments + SEM). Student test was performed to compare GSK343-treated to untreated cells. No significant difference was observed. **C,** Chromatin immunoprecipitation using an antibody against H3K27me3 or negative control rabbit IgG was performed on indicated cell lines. *Wnt11, Sema6d, Stmn2, Spock2* and *Spock3* genes were quantified by qPCR. Mean of 3 experiments (+ SEM). **D,** Quantification of cell adhesion 1 hour after seeding. Cells were pretreated with the 3µM GSK343 or vehicle for 5 to 7 passages (mean of 3 experiments + SEM). Student test was performed to compare GSK343-treated to untreated cells. No significant difference was observed.

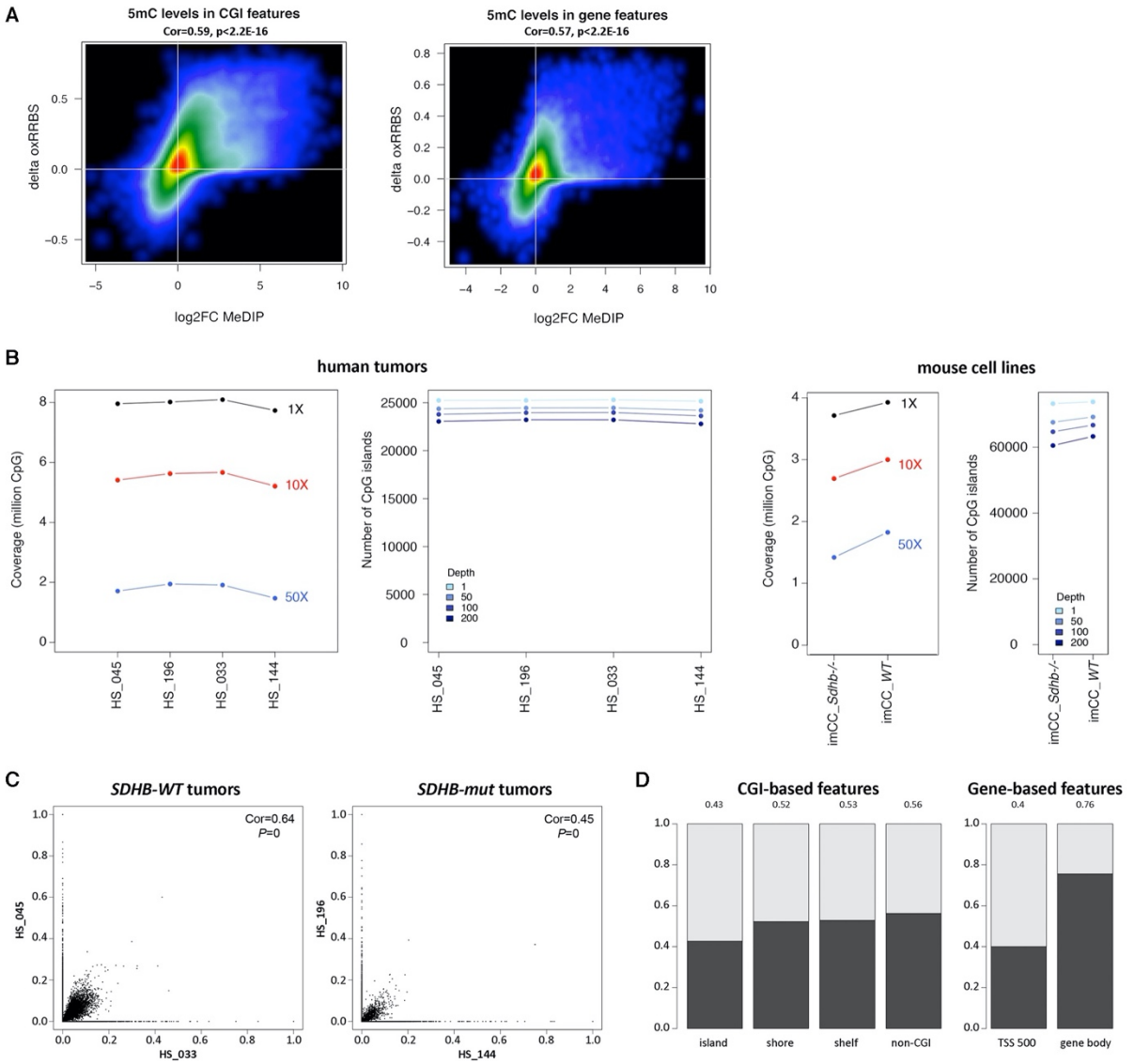


Figure S3. Related to Figure 3. Characteristics of genome-scale mapping of 5mC and 5hmC. A, Correlation of 5mC change between *SDHB*-mut and *SDHB*-WT tumors quantified by oxRRBS versus meDIP-seq. **B,** Coverage and sequencing depth of oxRRBS experiments in each tumor and cell line. **C,** 5hmC levels quantified by oxRRBS in each genomic feature. Correlation between tumors of same genotype. **D,** Proportion of features with detectable 5hmC (coverage >1000, positive value for RRBS-oxRRBS signal, and a significant q-value in at least one sample)

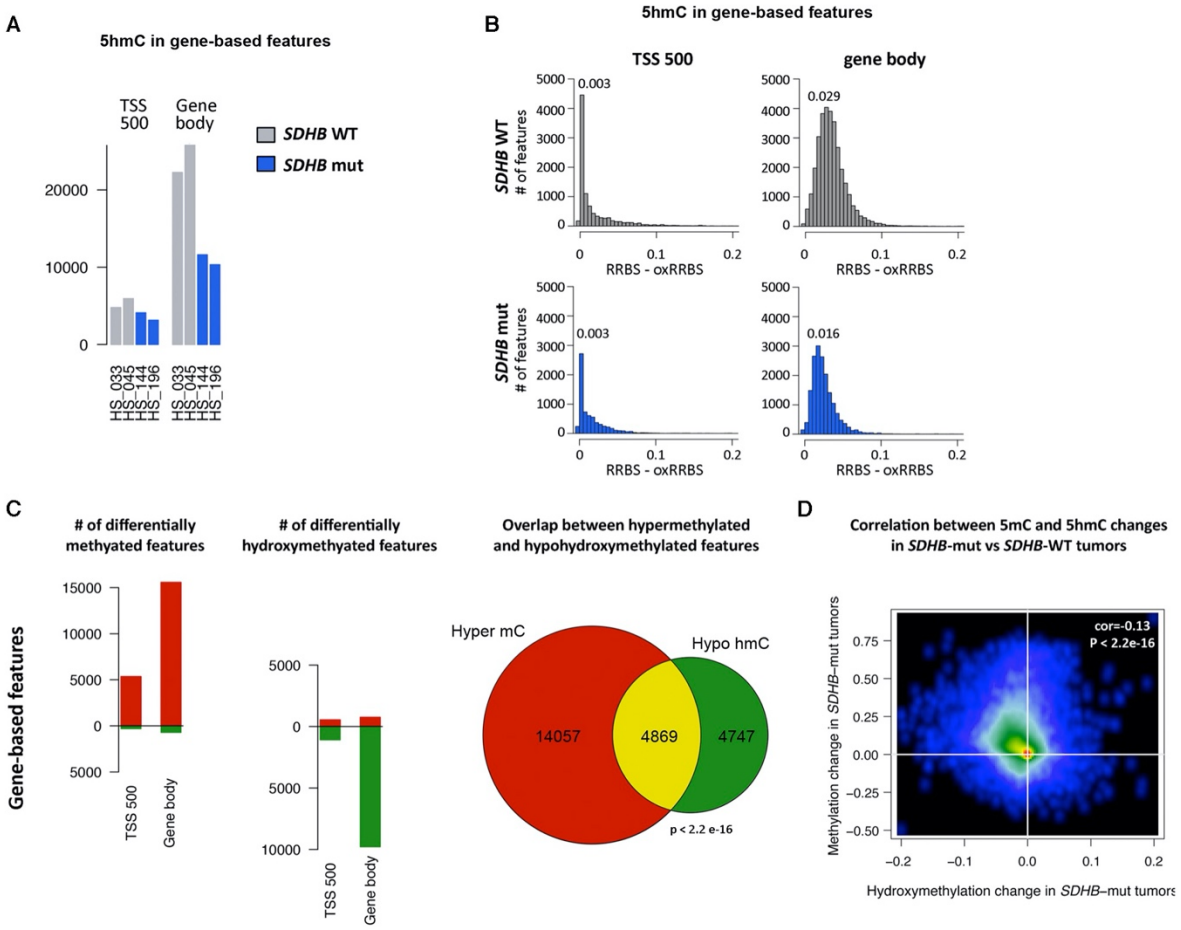


Figure S4. Related to Figure 3. 5-hmC detection in gene-based features in *SDHB*-mutated compared to *SDHB*-wild-type tumors. A, Number of regions in which 5hmC was detected. **B,** Distribution of 5hmC rates in regions where it was detected in *SDHB*-wild-type (top) or *SDHB*-mutated (bottom) tumors. **C,** Number and overlap of differentially methylated and hydroxymethylated regions in S*DHB*-mutated compared to *SDHB*-WT tumors. **D,** Correlation between delta-5mC and delta-5hmC in S*DHB*-mutated *vs SDHB*-WT tumors.

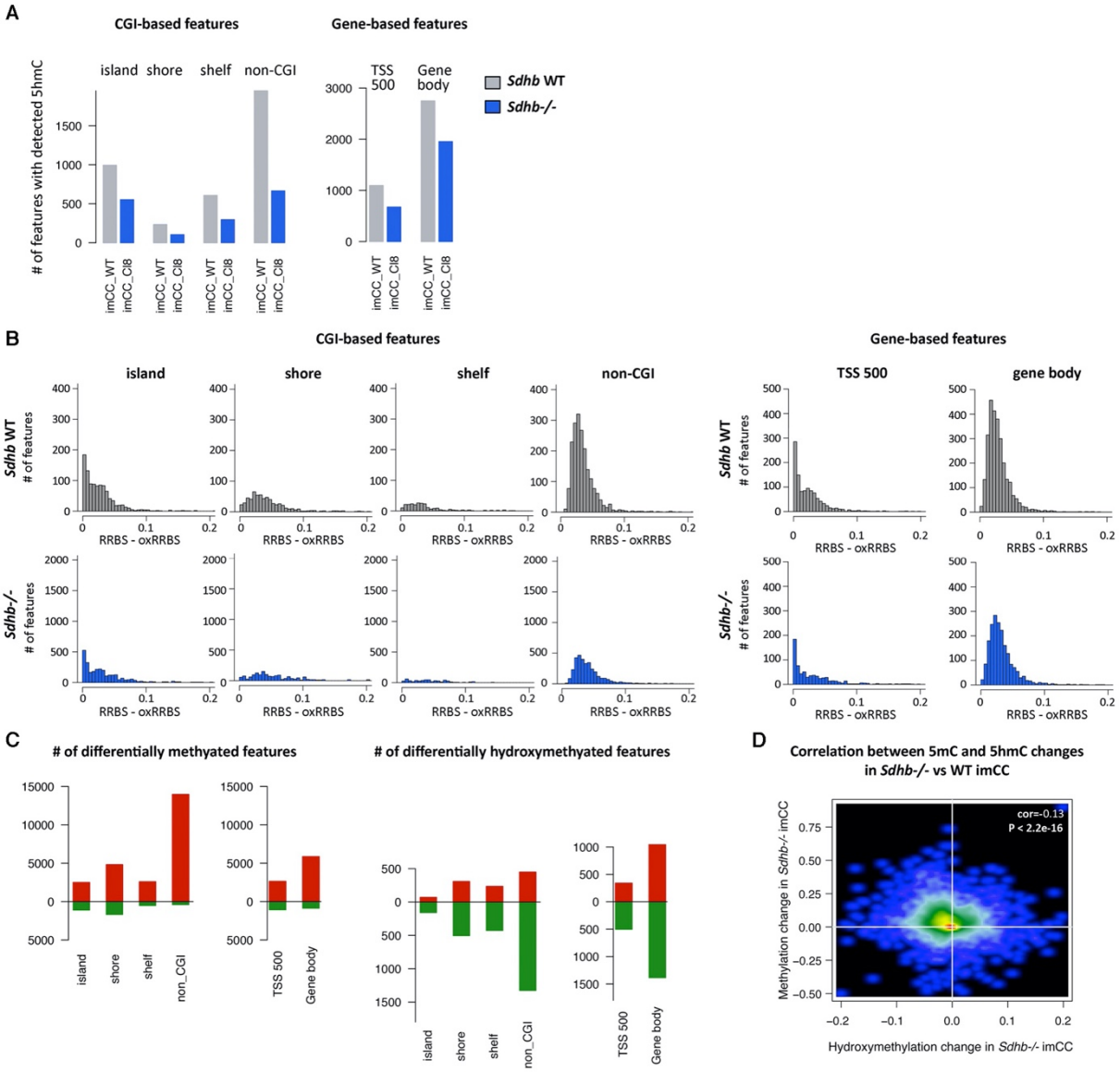


Figure S5. Related to Figure 3. 5-hmC detection in *Sdhb*-/- compared to *Sdhb*-wild-type imCC. A, Number of regions in which 5hmC was detected. **B,** Distribution of 5hmC rates in regions where it was detected in *Sdhb* WT (top) or *Sdhb*-/- (bottom) cells. **C,** Number of differentially methylated and hydroxymethylated regions in *Sdhb*-/- compared to *Sdhb*-WT cells. **D,** Correlation between delta-5mC and delta-5hmC in *Sdhb*-/- vs *Sdhb*-WT cells.

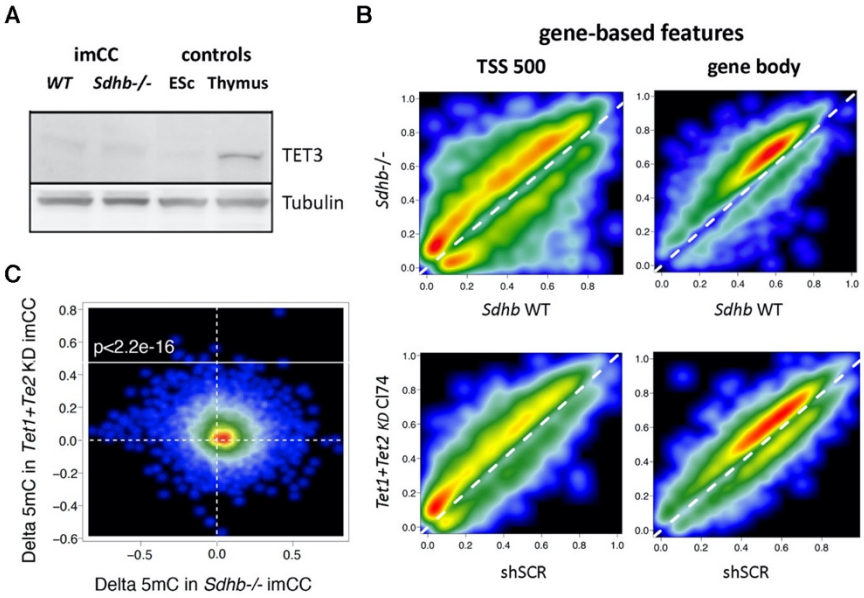


Figure S6. Related to Figure 5. Effects of *Tet1* and *Tet2* knock-down in imCC. A, Western blot analysis of TET3 in total protein extracts from imCC, mouse embryonic stem cells and mouse thymus. **B,** Smoothscatter plot from significantly differently methylated features in *Sdhb-/- vs Sdhb*-WT imCC (top) or *Tet1+Tet2*^{KD} *vs shSCR* imCC (bottom) **C,** Correlation of hypermerthylated gene-based features in *Tet1+Tet2*^{KD} *vs Sdhb-/-* imCC.

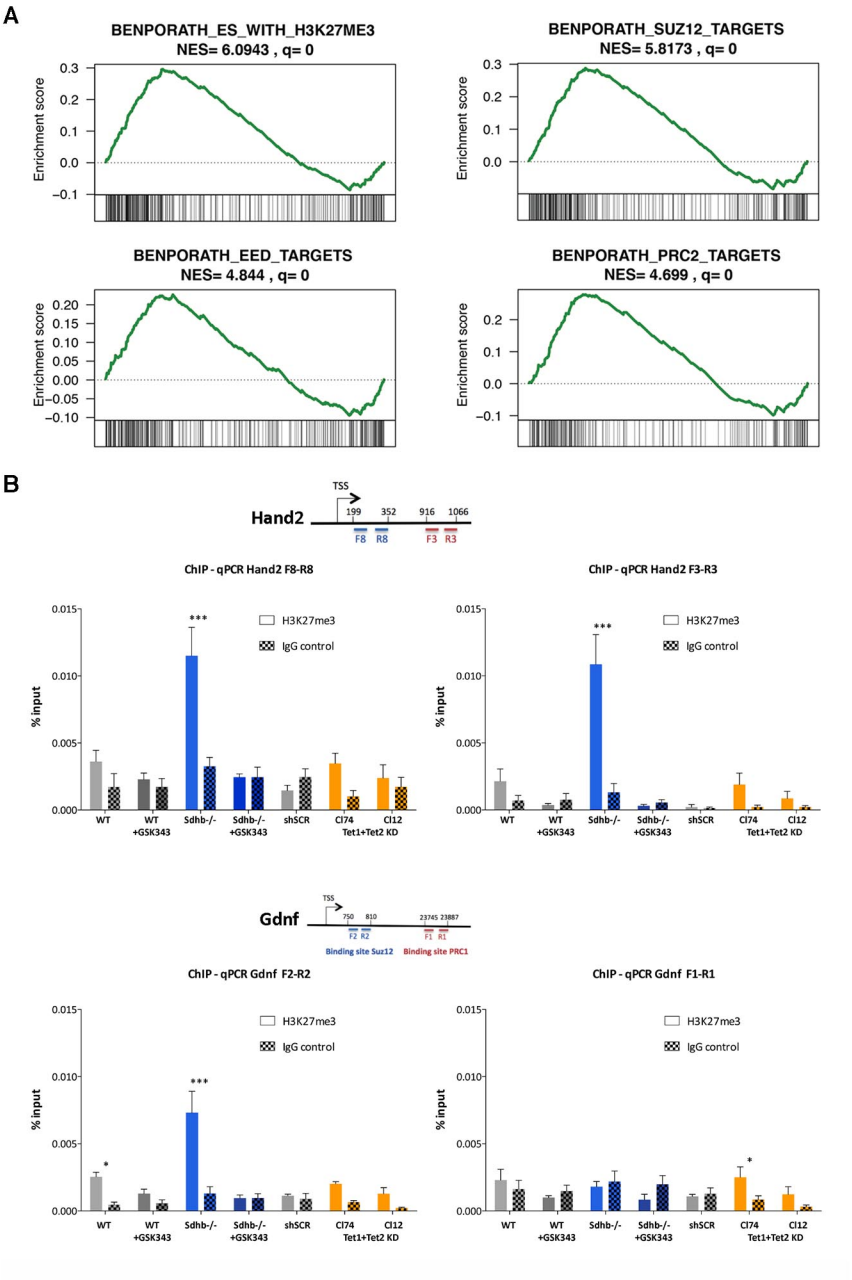


Figure S7. Related to Figure 5. PRC2 and TET have redundant targets in chromaffin cells. A, Hypermethylated genes in *Tet1+Tet2*^{KD} imCC compared to *shSCR* imCC are enriched in genes marked by H3K27me3 or targeted by SUZ12, EED or PRC2 in ES cells. **B,** Chromatin immunoprecipitation using an antibody against H3K27me3 or negative control rabbit IgG was performed on indicated cell lines. Hand2 and Gdnf genes were quantified by qPCR using 2 different primer pairs as indicated. Mean of 3 experiments (+ SEM). Student test was performed to compare H3K27me3 ChIP signal to background IgG signal.

Supplementary Table 2. Related to Figure 1: Number of features with detected 5hmC in human tumors

CGI-based features

	island.HS_033	island.HS_045	island.HS_144	island.HS_196	shore.HS_033	shore.HS_045	shore.HS_144	shore.HS_196	shelf.HS_033	shelf.HS_045	shelf.HS_144	shelf.HS_196
Number of features with sufficient coverage	23010	23010	23010	23010	32717	32717	32717	32717	21410	21410	21410	21410
Number of features with significant difference in oxRRBS	3003	4320	2789	2331	4689	6782	2141	1862	2670	4091	1165	915
Number of features with significant positive difference in oxRRBS	2599	3871	2125	1788	4448	6523	1795	1560	2562	3970	963	772
Proportion of good coverage features with significant positive difference	0.1129509	0.1682312	0.0923512	0.0777053	0.1359538	0.1993765	0.0548644	0.0476816	0.1196637	0.1854274	0.0449790	0.0360579

Gene-based features

	TSS500.HS_033	TSS500.HS_045	TSS500.HS_144	TSS500.HS_196	body.HS_033	body.HS_045	body.HS_144	body.HS_196
Number of features with sufficient coverage	46455	46455	46455	46455	58799	58799	58799	58799
Number of features with significant difference in oxRRBS	5880	7022	5629	4467	22645	26152	12425	10979
Number of features with significant positive difference in oxRRBS	4767	5939	4105	3145	22260	25767	11606	10329
Proportion of good coverage features with significant positive difference	0.1026154	0.1278442	0.0883651	0.0676999	0.3785779	0.4382217	0.1973843	0.1756663

Supplemental Table S3. Related to STAR Methods - Oligonucleotides

Ubc F	5′-AGCCCAGTGTTACCACCAAG-3′
Ubc R	5′-ACCCAAGAACAAGCACAAG-3′
18S F	5′-CGCGGTTCTATTTTGTTGGT-3′
18S R	5′-AACCATAAACGATGCCGAC-3′
B2m F	5’-ATTCACCCCCACTGAGACTG-3’
B2m R	5’-TGCTATTTCTTTCTGCGTGC-3’
Hand2 F	5’-CCAGCTACATCGCCTACCTC-3’
Hand2 R	5’-TGGTTTTCTTGTCGTTGCTG-3’
Gdnf F	5’-CTGTCTGCCTGGTGTTGCT-3’
Gdnf R	5’-CTGCCGCTTGTTTATCTGGT-3’
Wnt11 F	5’-TCCGATGCTCCTATGAAGGT-3’
Wnt11 R	5’-CTGACAGGTAGCGGGTCTTG-3’
Sema6d F	5’-GCTTCCCAGAAGACGATGAG-3’
Sema6d R	5’-CTGTTTGGGGGATTTCATTT-3’
Stmn2 F	5’-CTACGACGACATGGAGGTGA-3’
Stmn2 R	5’-CCTCTTCTCTGCCAACTGCT-3’
Spock2 F	5’-CCATCGGTTGGATGTTCTCT-3’
Spock2 R	5’-GACACCTGGCTTCTTCTTGG-3’
Spock3 F	5’-AGGATTCACTTGGCTGGATG-3’
Spock3 R	5’-TTTATCCCCTGTCGCTTCTG-3’
Snai1 F	5’-TGGAAAGGCCTTCTCTAGGC-3’
Snai1 R	5’-AAAAGCACGGTTGCAGTGG-3’
Twist1 F	5’-GACTCCAAGATGGCAAGCTG-3’
Twist1 R	5’-TTCTCTGGAAACAATGACATCTAGGT-3
Cdh2 F	5’-GAAGATGTTTACAGCGCAGTCTT-3’
Cdh2 R	5’-CTCGCTGCTTTCATACTGAACTT-3’
Epas1 F	5’-AGGGCCACAGCAAAGAGAG-3’
Epas1 R	5’-CATCACGGGATTTCTCCTTC-3’
Glut1 F	5’-AAACATGGAACCACCGCTAC-3’
Glut1 R	5’-GGAGAAGCCCATAAGCACAG-3’
Hif1a F	5’-TCAGCATACAGTGGCACTCA-3’
Hif1a R	5’-AAGGGAGCCATCATGTTCCA-3’
Hand2 F8	5’-GAAAATGGATGCGCTGAGAC-3’
Hand2 R8	5’-GTTCTTGGGCGCTTATTGTT-3’
Hand2 F3	5’-AAGGCGAGATGAGTCTGGTG-3’
Hand2 R3	5’-TAAGCCAGCCGTGGAAGTAG-3’
Gdnf F1	5’-TGGGCTATGAAACCAAGGAG-3’
Gdnf R1	5’-CAACATGCCTGGCCTACTTT-3’
Gdnf F2	5’-CTCTGGCCTTTTGCTTCAAC-3’
Gdnf R2	5’-CTAATCTCGACCCCGCATAA-3’
Wnt11 F	5’-GAGAGCCGAGCACAACTGAC-3’
Wnt11 R	5’-GCGAGGATAGCTTCTTCCAG-3’
Sema6d-Iso1 F	5’-TCCACAGAAGCGCCATAGAC-3’
Sema6d-Iso1 R	5’-GGGAGCTGAGAGCGTAACAC-3’
Sema6d-Iso2 F	5’-CTGTGGATGGTGCCTTGTT-3’
Sema6d-Iso2 R	5’-GACACCCTAGTAGCCGCTCA-3’
Stmn2 F	5’-GACCCTTCTCCTTTGCCTTC-3’
Stmn2 F R	5’-GATGTGCACGCACGGAGT-3’
Spock2 F	5’-ATTTCATGGAGGACGAGCAA-3’
Spock2 R	5’-TACTGCGAGATGGACGACAG-3’
Spock3 F	5’-TGGCTCACGACAATCTCTCA-3’
Spock3 R	5’-CGTCTCGGAATTTGTTCCAC-3’
Sdhb intron 1 Forward	5’-CTCATCGGGCTCCAGTTAAA-3’
Sdhb intron1 and loxP site reverse	5’-GCCGGCCATTTCTGACAC-3’

Supplemental Table S4. Related to Methods – Statistical section

figure	statistical test	n	analysis details	statistical details	Stastistical software
Fig 1 A - C. Fig 2 A		2 tumors / genotype	in Method section "MeDIP-seq analysis"	in figure legend	R statistical software
Fig1 D. Fig 2 B - C	enrichment score and nominal p-value	2 tumors / genotype	in Method section "Gene set enrichment analysis"	in Method section "Gene set enrichment analysis"	R code downloaded from the GSEA website
Fig 1 E	median with interquartile range	cohort of 113 genetically-determined PPGL tumors described in Letouze et al., 2013.	in Method section "RNA-seq analysis"	in figure legend	R statistical software and Bioconductor DESeq package
Fig 2 E	mean with SEM	3 independant experiments. In each experiment, 3 wells of each cell line. qPCR in triplicates.	in Method section "Reversed Transcription and Quantitative Real-Time PCR"	student test between treated and untreated cells: * p<0.05, ** p<0.001, *** p<0.0001	Graphpad Prism
Fig 2 F - G	mean with SEM	3 independant experiments. qPCR in triplicates.	in Method section "ChIP-qPCR"	student test: * p<0.05, ** p<0.001, *** p<0.0001	Graphpad Prism
Fig 2 I - J	logistic regression and the SLIM method for pvalue adjustment	1 RRBS experiment per treatment and cell type	in Method section "oxRRBS and RRBS Analyses"	in Method section "Differential (hydroxy)methylation analysis"	methylKit package (Akalin et al., 2012)
Fig 2 K	mean with SEM	3 independant experiments	in Method section "Wound scratch assay"	student test between treated and untreated cells: * p<0.05, ** p<0.001, *** p<0.0001	Graphpad Prism
Fig 3 & 5 C		Fig. 3: 4 tumor samples (2 SDHB-mutated and 2 SDHB-wt). Fig. 5C: 4 cell line samples (1 Sdhb wt, 1 Sdhb -/-, 1 sh_Scr, 1 sh_TET).	in Method section "oxRRBS and RRBS Analyses"	in Method sections "5hmC detection using (ox)RRBS data" and "Differential (hydroxy)methylation analysis"	Fisher's exact tests, corrected for multiple testing using Benjamini Hochberg procedure
Fig 3 D. Fig 4. Fig 5D	correlation	Fig. 3D and Fig. 4: 4 tumor samples (2 SDHB-mutated and 2 SDHB-wt). Fig. 5D: 4 cell line samples (1 Sdhb wt, 1 Sdhb -/-, 1 sh_Scr, 1 sh_TET).	in Method section "oxRRBS and RRBS Analyses" and "RNA-seq analysis"	Pearson correlation.	R statistical software
Fig 5 B	mean with SEM	3 independant experiments. ELISA in triplicates	in Method section "5mC and 5hmC ELISA"	student test between Sdhb-/- and WT and between shTet and shSCR cells: * p<0.05, ** p<0.001, *** p<0.0001	Graphpad Prism
Fig 5 E. Fig 6 C - D	mean with SEM	3 independant experiments. In each experiment, 3 wells of each cell line. qPCR in triplicates.	in Method section "Reversed Transcription and Quantitative Real-Time PCR"	student test between Sdhb-/- and WT and between shTet and shSCR cells: * p<0.05, ** p<0.001, *** p<0.0001	Graphpad Prism

Fig 5 F	mean with SEM	3 independant experiments	in Method section "Proliferation assay"	student test between Sdhb-/- and WT and between shTet and shSCR cells: * p<0.05, ** p<0.001, *** p<0.0001	Graphpad Prism
Fig 5 G	mean with SEM	3 independant experiments	in Method section "Adhesion assay"	student test between Sdhb-/- and WT and between shTet and shSCR cells: * p<0.05, ** p<0.001, *** p<0.0001	Graphpad Prism
Fig 5 H	mean with SEM	3 independant experiments	in Method section "Wound scratch assay"	student test between Sdhb-/- and WT and between shTet and shSCR cells: * p<0.05, ** p<0.001, *** p<0.0001	Graphpad Prism
Fig 6 E - F		119 tumors (SDH (n=23), VHL (n=40), NF1 (n=37) or RET (n=19))	in figure legend	hierarchical clustering was performed using the ClustVis software with default settings. https://biit.cs.ut.ee/clustvis/	
Fig 6 H	mean with SEM	3 independant experiments. ELISA in triplicates	in Method section "5mC and 5hmC ELISA"	student test between normoxic and hypoxic cells: no significative difference	Graphpad Prism
Fig 7 A	mean with SEM	3 independant experiments	in Method section "Proliferation assay"	student test between normoxic and hypoxic cells: * p<0.05, ** p<0.001, *** p<0.0001	Graphpad Prism
Fig 7 B	mean with SEM	3 independant experiments	in Method section "Adhesion assay"	student test between normoxic and hypoxic cells: * p<0.05, ** p<0.001, *** p<0.0001	Graphpad Prism
Fig 7 C	mean with SEM	3 independant experiments	in Method section "Wound scratch assay"	student test between normoxic and hypoxic cells: * p<0.05, ** p<0.001, *** p<0.0001	Graphpad Prism
Fig 7 E	mean with SEM	3 independant experiments. In each experiment, 3 wells of each cell line. qPCR in triplicates.	in Method section "Reversed Transcription and Quantitative Real-Time PCR"	student test between normoxic and hypoxic cells: * p<0.05, ** p<0.001, *** p<0.0001	Graphpad Prism
Fif 7 F	mean with SEM	Two different clones of *Tet1+Tet2 KD* imCC injected in 10 mice per clone, 5 mice for normoxic cells and 5 for hypoxic cells	in Method section "In vivo metastasis assay"	student test between normoxic and hypoxic cells: * p<0.05, ** p<0.001, *** p<0.0001	Graphpad Prism
Fig 8 A & C	mean with SEM	3 independant experiments. In each experiment, 3 wells of each cell line. qPCR in triplicates.	in Method section "Reversed Transcription and Quantitative Real-Time PCR"	student test relative to Sdhb-/- cells: * p<0.05, ** p<0.001, *** p<0.0001	Graphpad Prism
Fig 8 E	mean with SEM	3 independant experiments	in Method section "Proliferation assay"	student test relative to Sdhb-/- cells: * p<0.05, ** p<0.001, *** p<0.0001	Graphpad Prism
Fig 8 F	mean with SEM	3 independant experiments	in Method section "Adhesion assay"	student test relative to Sdhb-/- cells: * p<0.05, ** p<0.001, *** p<0.0001	Graphpad Prism
Fig 8 G	mean with SEM	3 independant experiments	in Method section "Wound scratch assay"	student test relative to Sdhb-/- cells: * p<0.05, ** p<0.001, *** p<0.0001	Graphpad Prism